國立交通大學

電機學院 IC 設計產業研發碩士班

碩 士 論 文

超 寬 頻 人 體 區 域 網 路 之 無 線 電 通 道 探 討 與 建 構

Radio Channels Characterization and Modeling of UWB Body Area Networks

研 究 生：彭思云

指導教授：唐震寰　教授

中 華 民 國 九 十 六 年 七 月

超寬頻人體區域網路之無線電通道探討與建構
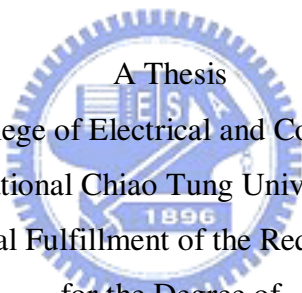# Radio Channels Characterization and Modeling of UWB Body Area Networks

研 究 生：彭思云   Student：Szu-Yun Peng

指導教授：唐震寰   Advisor：Jenn-Hwan Tarng

國 立 交 通 大 學
電機學院 IC 設計產業研發碩士班
碩 士 論 文

A Thesis

Submitted to College of Electrical and Computer Engineering

National Chiao Tung University

in partial Fulfillment of the Requirements

for the Degree of

Master

in

Industrial Technology R & D Master Program on
IC Design

July 2007

Hsinchu, Taiwan, Republic of China

中華民國九十六年七月

超寬頻人體區域網路之無線電通道探討與建構

學生：彭思云　　　　　　　　　　　　　　指導教授：唐震寰

國立交通大學電機學院產 IC 設計業研發碩士班

摘　　　要

　　應用於超寬頻單輸入單輸出人體區域網路通道建構，由時間響應可觀察出在空曠的環境中繞射波為主要的傳播路徑，但在有許多散射體的環境下，接收端擺放在身體後面，散射體所引起的散射波成為主要的傳播機制。收到的信號強度也會比在沒有散射體的環境下來得強。因此在有許多散射體的空間中，路徑散逸指數會比空曠環境小。赤池信訊息量準則 (Akaike Information Criterion) 指出對數常態分佈是最適合用來模擬小尺度衰減。

　　應用於超寬頻多輸入多輸出人體區域網路通道量測，接收端天線陣列放置於身體背部的通道容量會高於接收端放置在身體的前端。是因為身體擋掉接收端的訊號，減少接收端天線的相關性。多輸入多輸出人體區域網路系統的容量受環境影響不大。但是，接收端放置在身體前端比起放置在後端比較容易受當地的環境影響。我們可以發現當天線空間增加時通道容量減少，是因為即使傳送端與接收端的天線空間增加也許會使得相關性降低導致容量增加，但是由於繞射波大幅降低使得次通道的訊號強度會被削弱，次通道沒有貢獻。因此，天線之間的空間增加也許不會對通道容量有所貢獻。

Radio Channels Characterization and Modeling of UWB Body Area Networks

student：Szu-Yun Peng   Advisor：Dr. Jenn-Hwan Tarng

Industrial Technology R & D Master Program on IC Design
of   Electrical and Computer Engineering College
National Chiao Tung University

ABSTRACT

For channel modeling of UWB SISO BAN, it is found that the diffracted wave is the dominant propagation path in the open space observed from the temporal response. However, when the Rx places on the back of the body that is surrounded by dense local scatterers, the scattering due to the local scatterers becomes the dominant propagation mechanism and the received signal strength is much larger than that of without local scatterers. Therefore, the path loss exponent in the room with dense local scatterers is smaller than that in open space. The AIC indicates that the Lognormal distribution is the best one in modeling the small scale fading distribution.

For MIMO BAN measurement, the capacity of Rx antenna array elements placed on the back of the body is higher than that placed on the front of the body. This is due to the received signal obstructed by the body, which yields reduction of the spatial channel correlation at the Rx antenna. The influence of environment on the capacity of BAN MIMO system is not significant. However, the capacity of Rx placed on the front of the body is more easy affected by the local environment than that placed on the back of the body. It is found that the capacity of the MIMO BAN decreases as the element spacing increases. It is because that although the increasing element spacing may reduce the correlation of Rx or Tx and leads capacity increase, the signal strength of the subchannel decreases a lot due to large diffraction loss and yields little contribution of the subchannel. Therefore, element spacing increases may not contribute to the MIMO channel capacity.

誌謝

首先誠摯的感謝指導教授唐震寰博士，老師悉心的教導使我得以一窺 超寬頻人體區域網路之無線電通道建構 領域的深奧，不時的指導並指點我正確的方向，使我在這兩年中獲益匪淺。老師對學問的嚴謹更是我輩學習的典範。

本論文的完成另外亦得感謝台灣科技大學的王威翔及王釗偉同學大力協助，因為有你們的體諒及幫忙，使得本論文能夠更完整而嚴謹。

兩年裡的日子，實驗室裡共同的生活點滴，學術上的討論、言不及義的閒扯、讓人又愛又怕的宵夜、趕作業的革命情感........，感謝眾位學長、同學、學弟的共同砥礪，你們的陪伴讓兩年的研究生活變得絢麗多彩。

感謝維儒、秉文、文崇學長們不厭其煩的指出我研究中的缺失，且總能在我迷惘時為我解惑，也感謝志瑋、育正、奕慶、豐吉同學們及超麻吉好友蓓縝的幫忙，恭喜我們順利走過這兩年。實驗室的雅仲、俊彥學弟們當然也不能忘記，你們的幫忙及搞笑我銘感在心。

最後，謹以此文獻給我摯愛的雙親及家人。

彭思云

民國 96 年 7 月 新竹

CONTENTS

LIST OF TABLES

LIST OF FIGURES

Chapter 1   *Introduction*

1.1   Background and Problems

Using wireless sensors around the body to monitor health information is a promising new application made possible by recent advances in ultra low power technology. Each sensor placed on human body or in close proximity such as everyday clothing continuously measures parameters of interest and sends the data to a central device such as personal digital assistant (PDA).The large diversity and potential of these applications makes it an exciting new research direction in wireless communications.

The IEEE 802.15.4a committee is developing a low-power UWB standard and includes body area networks (BANs) as a relevant scenario [1]. The Task Group 802.15.4a has the mandate to develop an alternative physical layer for sensor networks and similar devices, working with the IEEE 802.15.4 MAC layer. The main goals of this new standard are energy-efficient data communication with data rates between one Kbit/s and several Mbit/s. More details about the goals of the task group can be found in

the IEEE 802.15.4a PAR [1]. The Federal Communications Commission (FCC) has recently legalized a spectral mask between 3.1-10.6GHz for UWB radios.

1.2 Related Works

UWB radio channel characterization and modeling of Body area networks have been presented in the following literatures. In [2], electromagnetic wave propagating around a human body is simulated with a finite-difference time-domain (FDTD) simulator at 2.4GHz. It is found that the main mechanism of wave propagation around the body is via creeping waves, which can be modeled a single path. For simplification, a dual-slope model can be used to describe the averaged path loss. In [3], body area channel consists of the initial cluster of components diffracting around the body, followed by subsequent clusters of components reflecting off of surrounding object in the office. The channel described by a high path loss exponent at 3 – 6 GHz, and the Multipath components cluster is modeled by Lognormal distribution. Ref. [4] focus on transmission at the head, the attenuation of the head is about 5 – 10 dB at 1.5 – 8 GHz. The measurement result illustrate that head is absorbing most energy that is transmitted into its direction, and the diffraction is the dominant propagation mechanism around the head. In [5], the components diffracting around the body are well modeled using correlated lognormal distribution and Nakagami-m distribution can be use to incorporate the influence of arm motion.

1.3 Motivation

Most literatures only focus on 3-6 GHz band and measure in indoor environments. In order to consider UWB frequency band completeness, measuring at 3.1 - 6, 6 – 10, and

3.1 – 10 GHz bands makes the whole measurement and the model in the integrity. Except the indoor environment with plenty scatterers, measuring the body in the open space and space with little scaterers can get more channel characterizations.

To extend our result, not only to characterize and model the BAN UWB channel for Single-input, Single-output (SISO) application, we also the explore MIMO case.

1.4 Organization

The thesis is organized into six chapters including the introduction. Chapter 2 gives an overview of the body area network propagation channel models, and definitions of the channel parameters that will be used in later chapters. Chapter 3 introduces ultra-wideband antenna implementation and measurement environment. Chapter 4 construct the path loss model and analysis the measured results for BANs. Chapter 5 describes the characterization of UWB MIMO radio channels. Chapter 6 concludes the thesis and improvements are suggested for future work.

Chapter 2 *Fundamental Theory of UWB Body Area Networks Propagation Channel Models*

2.1 Path Loss Model

Both theoretical and measurement-based propagation models indicate that average received signal power decreases logarithmically with distance, whether in outdoor or indoor radio channels. Such models have been used extensively in the literature. The average large-scale path loss for an arbitrary T-R separation is expressed as a function of distance by using a path loss exponent, n

$$\overline{PL}(d) \propto (\frac{d}{d_0})^n \tag{2.1}$$

Or

$$\overline{PL}(dB) = \overline{PL}(d_0) + 10n\log(\frac{d}{d_0}) \tag{2.2}$$

Where n is the path loss exponent which indicates the rate at which the path loss increases with distance, d_0 is the close-in reference distance which is determined from measurements close to the transmitter, and d is the T-R separation distance. The bars in Equations (2.1) and (2.2) denote the ensemble average of all possible path loss values for a given value of d. Where plotted on a log-log scale, the modeled path loss is a straight line with a slope equal to $10n$ dB per decade.

Table 2.1 Path loss exponents for different environments

Environment	Path Loss exponent, n
Free space	2
Urban area cellular radio	2.7 to 3.5
Shadowed urban cellular radio	3 to 5
In building line-of-sight	1.6 to 1.8
Obstructed in building	4 to 6
Obstructed in factories	2 to 3

The value of n depends on the specific propagation environment. For example, in free space, n is equal to 2, and when obstructions are present, n will have a larger value. It is important to select a free space reference distance that is appropriate for the propagation environment. Table 2.1 lists typical path loss exponents obtained in various mobile radio environments.

2.2 Small Scale Distribution

2.2.1 Rayleigh Fading

When the composite received signal consists of a large number of plane waves, the received envelope has a Rayleigh distribution, i.e.

$$p_z(x) = \frac{x}{\sigma^2} \exp\left\{-\frac{x^2}{2\sigma^2}\right\}$$

(2.3)

For a Rayleigh distributed envelope, the average power is $\Omega_p = 2\sigma^2$, so that

$$p_z(x) = \frac{2x}{\Omega_p} \exp\left\{-\frac{x^2}{\Omega_p}\right\}$$

(2.4)

Rayleigh fading usually applies to any scenario where there is no LOS path between the transmitter and receiver antennas.

2.2.2 Nakagami –m Fading

The Nakagami distribution was selected to fit empirical data, and is known to provide a closer match to some experimental data than either the Rayleigh, or Ricean distributions. In essence, the Nakagami distribution describes the received envelope, i.e.

$$p_z(x) = \frac{2m^m x^{2m-1}(K+1)}{\Gamma(m)\Omega_p^m} \exp\left\{-\frac{mx^2}{\Omega_p}\right\} \quad m \geq \frac{1}{2}$$

(2.5)

The Nakagami distribution is often used to model multipath fading for the following reasons. First, the Nakagami distribution can model fading conditions that are either more or less severe than Rayleigh fading. When m=1, the Nakagami distribution becomes the Rayleigh distribution, when m=1/2 it becomes a one-sided Gaussian distribution. Second, the Rice distribution (which does have physical significance) can

be closely approximated by using the relation $m = \dfrac{(K+1)^2}{(2K+1)}$, between the Rice factor K

and Nakagami parameter m.

2.2.3 Lognormal Distribution

The log-normal distribution is the probability distribution of any random variable whose logarithm is normally distributed. If X is a random variable with a normal distribution, then exp(X) has a log-normal distribution.

A variable might be modeled as log-normal if it can be thought of as the multiplicative product of many small independent factors. For example the long-term return rate on a stock investment can be considered to be the product of the daily return rates.

The log-normal distribution has the probability density function

$$f(x;\mu,\sigma) = \frac{e^{-(ln\,x - \mu)^2 /(2\sigma^2)}}{x\sigma\sqrt{2\pi}} \tag{2.6}$$

For x > 0, where μ and σ are the mean and standard deviation of the variable's logarithm (by definition, the variable's logarithm is normally distributed).

2.2.4 Weibull Distribution

The Weibull distribution is a probability distribution with the probability density function

$$\text{c} \qquad\qquad f(x;k,\lambda) = \frac{k}{\lambda}(\frac{x}{\lambda})^{k-1} e^{-(x/\lambda)^k} \tag{2.7}$$

For $x \geq 0$ and f(x; k, λ) = 0 for x < 0, where k > 0 is the shape parameter and λ >

0 is the scale parameter of the distribution.

The Weibull distribution is often used in the field of life data analysis due to its flexibility—it can mimic the behavior of other statistical distributions such as the normal and the exponential. If the failure rate decreases over time, then k < 1. If the failure rate is constant over time, then k = 1. If the failure rate increases over time, then k > 1.

2.2.5   Exponential Distribution

The exponential distributions are a class of continuous probability distribution. They are often used to model the time between independent events that happen at a constant average rate.

The probability density function (pdf) of an exponential distribution has the form

$$f(x;\lambda) = \begin{cases} \lambda e^{-\lambda x} & , x \geq 0, \\ 0 & , x < 0. \end{cases} \tag{2.8}$$

where $\lambda > 0$ is a parameter of the distribution, often called the rate parameter.

2.2.5 Akaike Information Criterion

Akaike's an information criterion (AIC) is a measure of the goodness of fit of an estimated statistical model. It is grounded in the concept of entropy. The AIC is an operational way of trading off the complexity of an estimated model against how well the model fits the data. In the general case, the AIC is

$$AIC = 2k - 2ln(\,L\,) \tag{2.9}$$

where k is the number of parameters, and L is the likelihood function.

Over the remainder of this entry, it will be assumed that the model errors are normally and independently distributed. Let n be the number of observations and RSS be the residual sum of squares. Then AIC becomes

$$AIC = 2k + n\,ln(\,RSS\,/\,n\,) \tag{2.10}$$

Increasing the number of free parameters to be estimated improves the goodness of fit, regardless of the number of free parameters in the data generating process. Hence AIC not only rewards goodness of fit, but also includes a penalty that is an increasing function of the number of estimated parameters. This penalty discourages overfitting. The preferred model is the one with the lowest AIC value. The AIC methodology attempts to find the model that best explains the data with a minimum of free parameters.

2.3 Generalized UWB-MIMO Capacity Formula

Consider a UWB-MIMO system with M transmits elements and N receives elements. The baseband input-output relationship is given by

$$\vec{y}(\tau) = \bar{H}(\tau) \times \vec{s}(\tau) + \vec{n}(\tau) \tag{2.11}$$

where $\vec{s}(\tau)$ is the transmitted signal, $\vec{y}(\tau)$ is the receiver signal, $\vec{n}(\tau)$ is AWGN (Additive White Gaussian Noise) and $\times$ denotes convolution. Each element of the channel impulse response matrix $\bar{H}(\tau)$ is the impulse response from a transmit

antenna to a receiver antenna.

When the transmitted power is equally allocated to each transmit element and frequency subchannel, the UWB-MIMO channel capacity can be expressed as [17], [31]

$$C = \frac{1}{W} \int_W \log_2 \det\left(I_{n_R} + \frac{\rho}{n_T} H(f)H^*(f) \right) df \qquad \text{bits/s/Hz} \qquad (2.12)$$

where n_T and n_R are the numbers of Tx and Rx antenna array elements, respectively, and W is the overall bandwidth of the MIMO channel, $H(f)$ is the normalized frequency response matrix of each narrow-band subchannel, * is the complex conjugate, and ρ is the average SNR at each receiver branch over the entire bandwidth. Since the measured UWB-MIMO matrices include the pathloss, we have to do a normalization to set the average receiver SNR to a specific value. Here, we normalize the frequency response of every narrow-band subchannel using a common factor such that

$$\int_W E\left(\|H(f)\|_F^2\right) df = W n_T n_R \qquad (2.13)$$

We also write capacity formula into another form [10]

$$C_i = \frac{1}{N_f} \sum_f^{N_f} \log_2\left(\det\left(I_{N_R} + \frac{\rho}{n_T} H_{i,f} H_{i,f}^* \right) \right) \qquad \text{bits/s/Hz} \qquad (2.14)$$

where N_f is frequency components and i is the time or snapshot index.

The normalization factor for each UWB-MIMO measurement snapshot T_i *(i is the time or snapshot index)* was calculated separately. This removed the effect of large-scale spatial fading, which can be significant for dynamic measurements, and ensured that only the small-scale: spatial fading was observed. T_i has dimensions of $n_R \times n_T \times N_f$,

where n_R, n_T, N_f are the number of receive antennas, transmit antennas and frequency components respectively. Each 5x5 measured channel snapshot had dimensions of $(5 \times 5 \times 801)$, thus providing a sufficient number of independent samples for normalization. The normalized UWB-MIMO channel H_i was calculated from (2-8) and (2-9), where $\hat{\eta}_k$ is the normalization factor estimate.

$$H_i = \frac{T_i}{\hat{\eta}_k} \qquad (2.15)$$

$$\hat{\eta}_k^2 = \frac{1}{n_R n_T N_f} \sum_{f=1}^{N_f} \sum_{j=1}^{n_R} \sum_{k=1}^{n_T} |T_{i,f,j,k}|^2 \qquad (2.16)$$

The goal of channel normalization is usually to scale the channel response so that the expectation of its power is unity. We refer to this as *unity-gain* normalization.

2.4 Complex Spatial Correlation Coefficient

In addition to capacity, we also considered the correlation at both transmit and receive side. To estimate the receive and transmit correlation matrix we let h_{ij} be the channel complex gain between j-th Tx element and i-th Rx element. The complex correlation coefficient between h_{ij} and h_{kl} is given as [21]

$$\rho(a,b) = \frac{E[ab^*] - E[a]E[b^*]}{\sqrt{E[|a|^2 - |E[a]|^2]E[|b|^2 - |E[b]|^2]}} \qquad (2.17)$$

where * denotes the complex conjugate operation and $a = h_{ij}$ and $b = h_{kl}$. The complex correlation coefficient is a complex number that is less than unity in absolute value. In the following figures we will only present its absolute value. Also, it is assumed that all antenna elements in the two arrays have the same polarization and the same radiation

pattern. To describe the propagation environments around Tx and Rx, the correlation coefficients of Tx and Rx are explored and given by [21], respectively,

$$\rho_{Tx} = \rho(h_{ij}, h_{il}) \tag{2.18}$$

$$\rho_{Rx} = \rho(h_{ij}, h_{kj}) \tag{2.19}$$

Receiver correlation describes the local scattering around the receivers, whereas transmitter correlation describes the correlation of the transmitted signals as seen at the receiver and does not provide insight into the scattering of the environment close to the transmitter array.

It is noted that ρ_{Tx} and ρ_{Rx} are first averaged over the index elements (j, l) or (I, k) then over the element indices i (receiving elements) and j (transmitting elements) respectively.
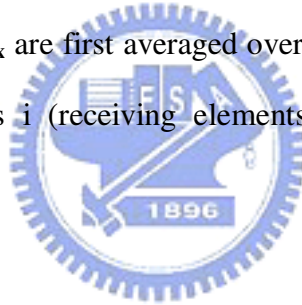
Chapter 3　　*Measurement System and Scenarios*

3.1 UWB Antenna Implementation and Measurement

Here we follow the design done by [7] to implement an UWB antenna for BAN channel measurement. Figure 3.1 illustrates the UWB antenna, which is a modified bow-tie antenna using a binomial function to describe its contour. The binomial function can be represented as:

$$f(x) = \begin{cases} g & x = 0 \\ g + L\left(\dfrac{x}{W}\right)^N & 0 < x < x_0 \\ g + L & x = x_0 \end{cases} \tag{3.1}$$

The antenna is fabricated using FR4 dielectric material (thickness = 0.8 mm, dielectric constant = 4.4) and analyzed by using Ansoft HFSS. Length and width of the bow-tie antenna is 20 mm and 30 mm, respectively. Length and width of the ground plane is 50 mm and 52 mm, respectively. $N = 4$ is set for the binomial function to yield optimal performance [7].
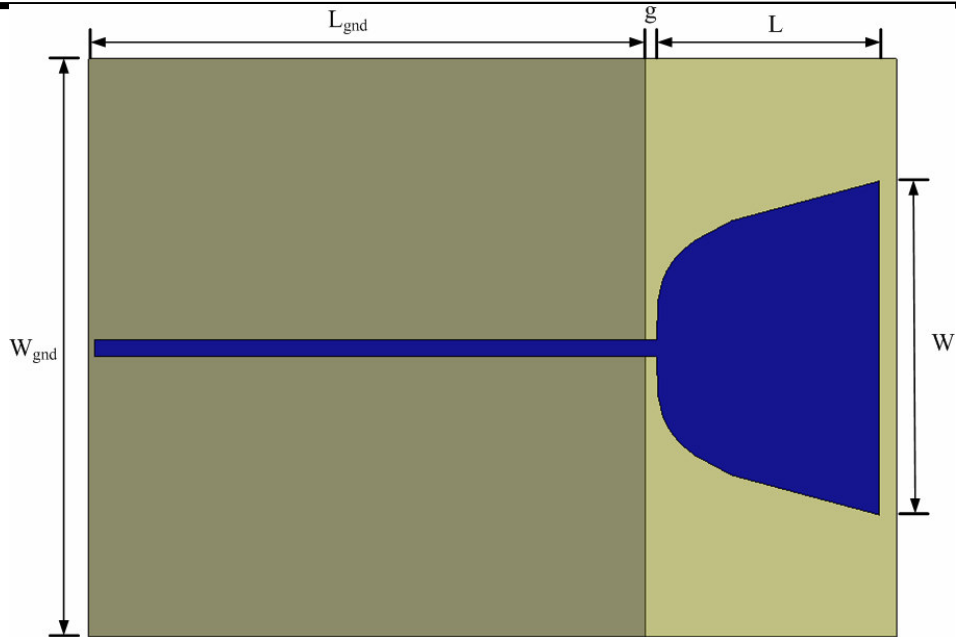
Figure 3.1 The geometry of the modified bow-tie antenna.
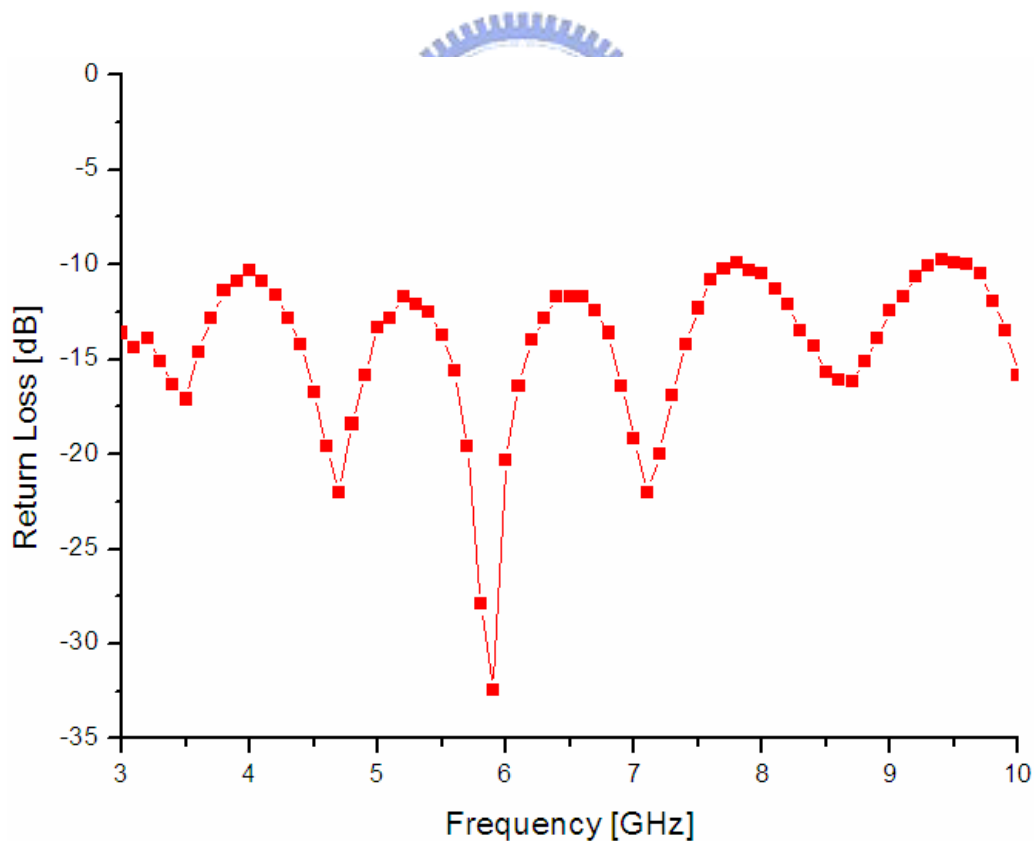
Figure 3.2 Measured return loss versus frequency.

Figure 3.2 shows the measured return loss versus frequency of the antenna. The antenna shows good performance in the range of 3 – 10 GHz. Figures 3.3, 3.4, and 3.5

are its measured far-field radiation patterns of x-z, y-z and x-y planes, respectively. The radiation pattern is omni-directional. Figure 3.6 is its measured near-field patterns of x-z plane.

(a)

(b)   (c)
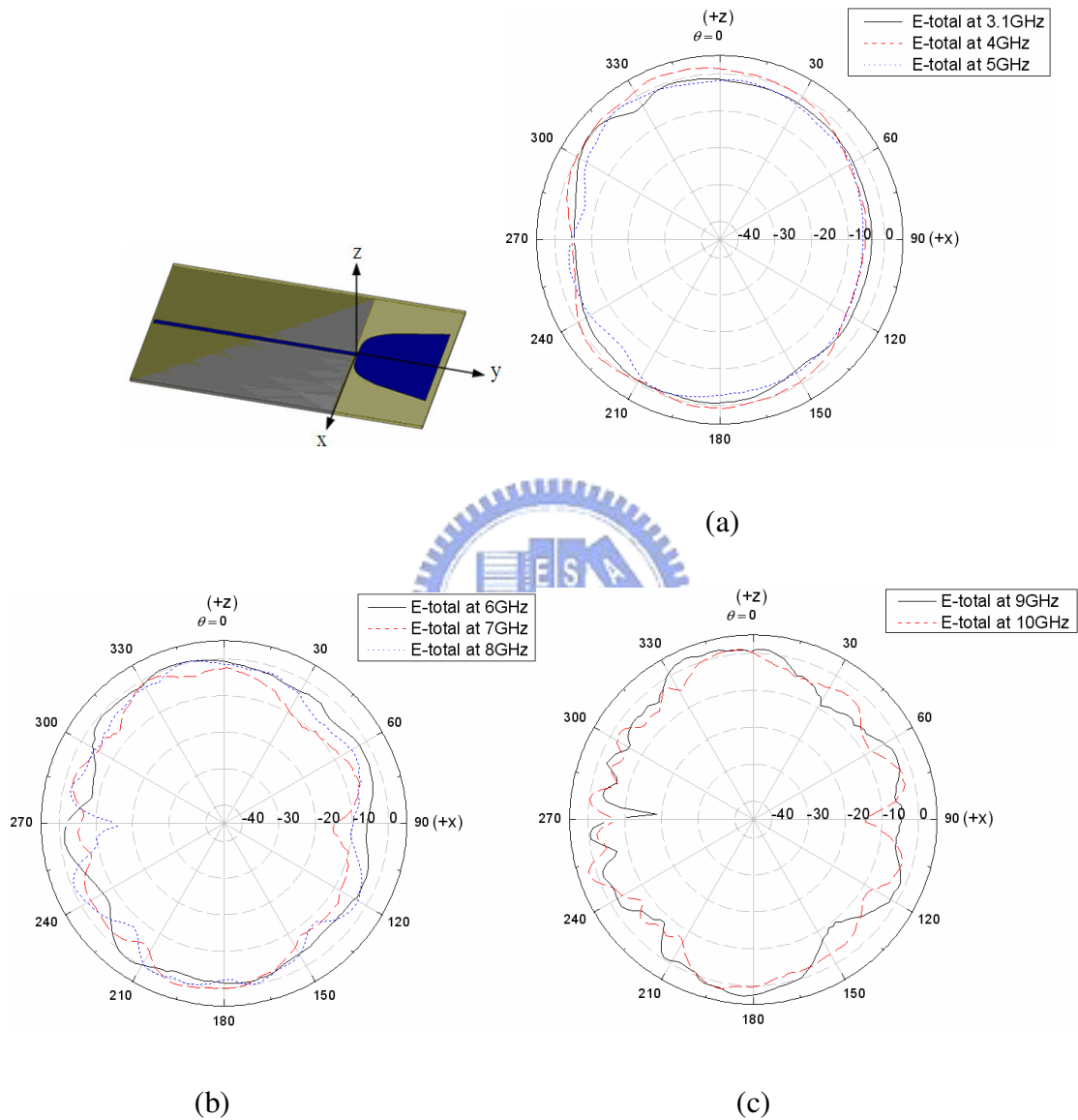
Figure 3.3 Measured far-field radiation pattern in the x-z plane (a) E-total at 3.1, 4, and 5 GHz (b) E-total at 6, 7, and 8 GHz (c) E-total at 9 and 10 GHz.

(a)

(b)

(c)
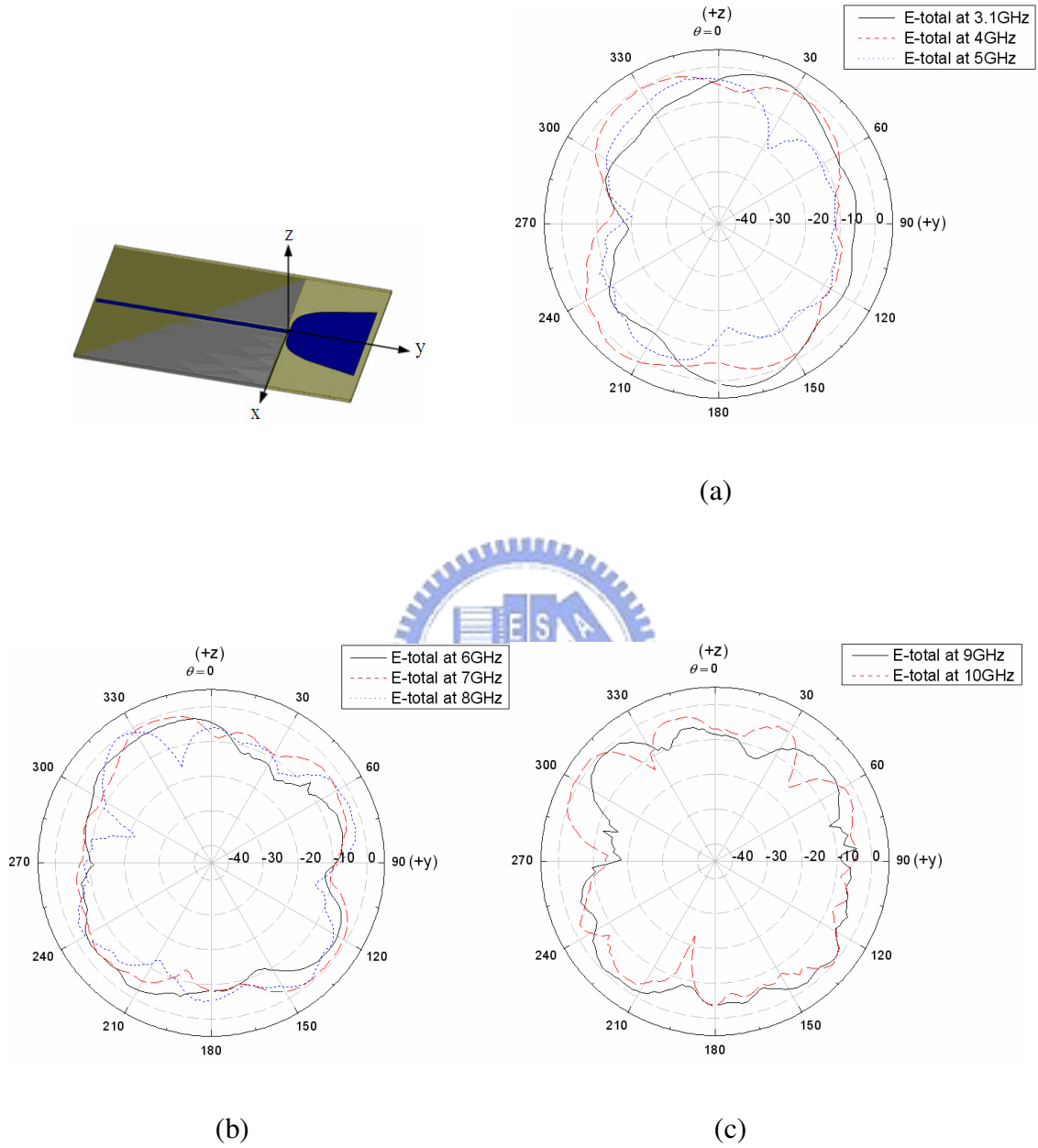
Figure 3.4 Measured far-field radiation pattern in the y-z plane (a) E-total at 3.1, 4, and 5 GHz (b) E-total at 6, 7, and 8 GHz (c) E-total at 9 and 10 GHz.

(a)

(b)

(c)
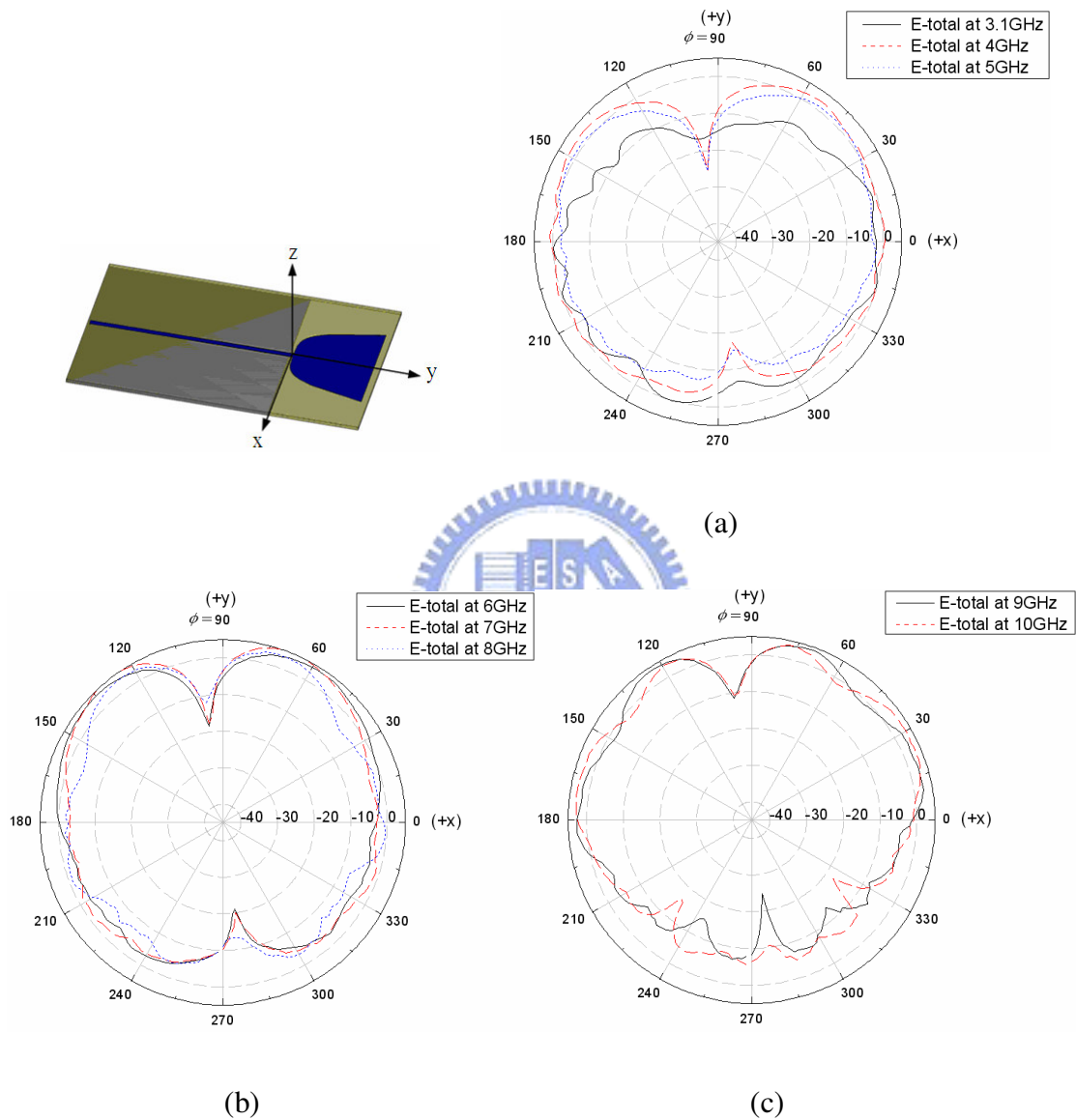
Figure 3.5 Measured far-field radiation pattern in the x-y plane (a) E-total at 3.1,4, and 5GHz (b) E-total at 6, 7, and 8 GHz (c) E-total at 9 and 10 GHz.

(a)

(b)

(c)

(d)
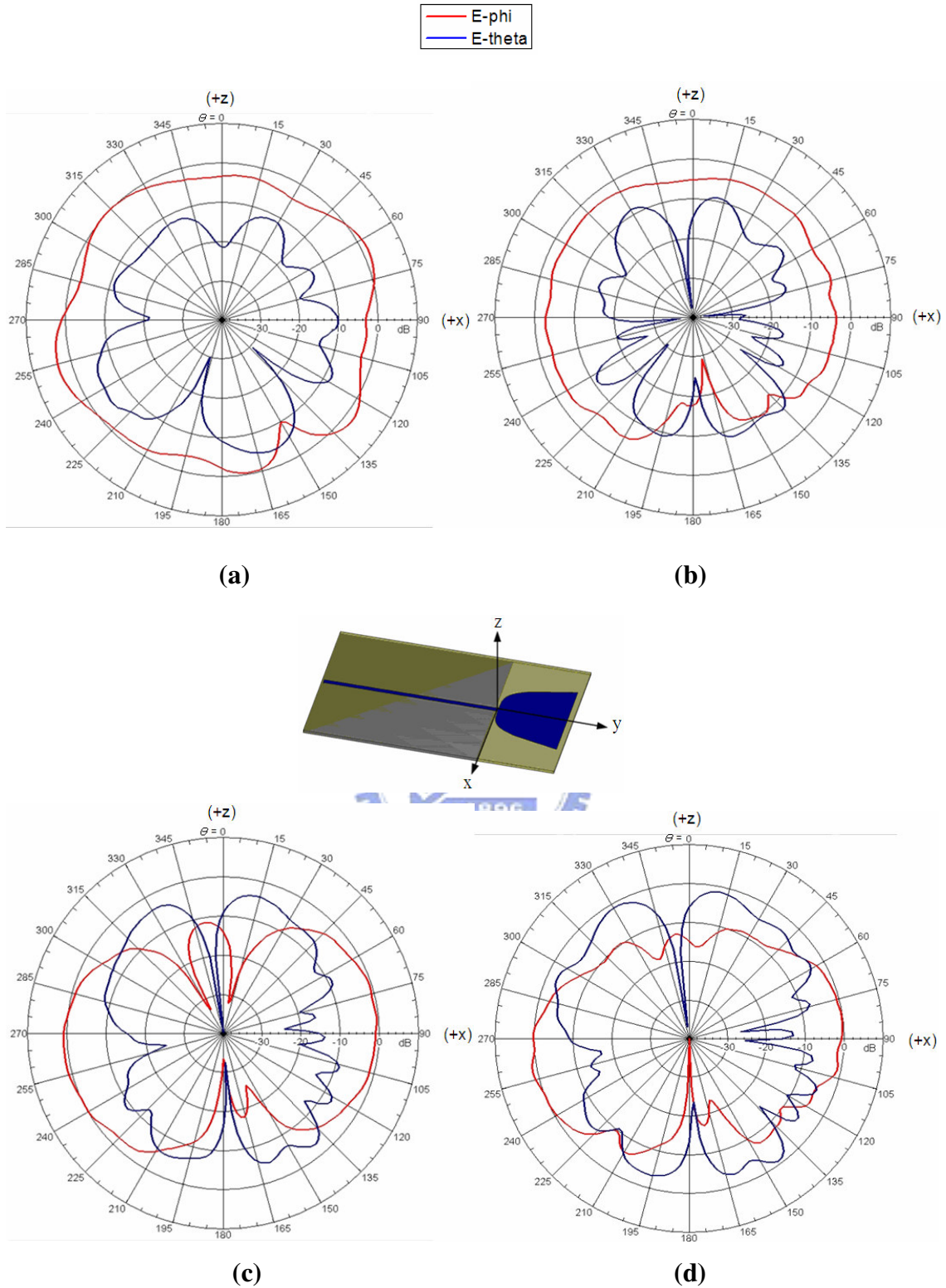
Figure 3.6 Measured near-field pattern in the x-z plane at (a) 3.1 GHz, (b) 8 GHz, (c)9 GHz, and (d)10 GHz.

In order to explore the influence of antenna radiation patterns by human bodies, the near and far fields of an UWB antenna near a plastic bottle full of normal saline are measured in the chamber. Figure 3.7 illustrates a picture of near-field measurement set-up. The measurement chamber is located in Wireless Communications & Applied Electromagnetics LAB of the National Taiwan University of Science and Technology.

Compare with Figure 3.5 and Figure 3.10, it indicates that the radiation is fluctuated by the human body. It is noted that there are strong fluctuation in the x-y plane.
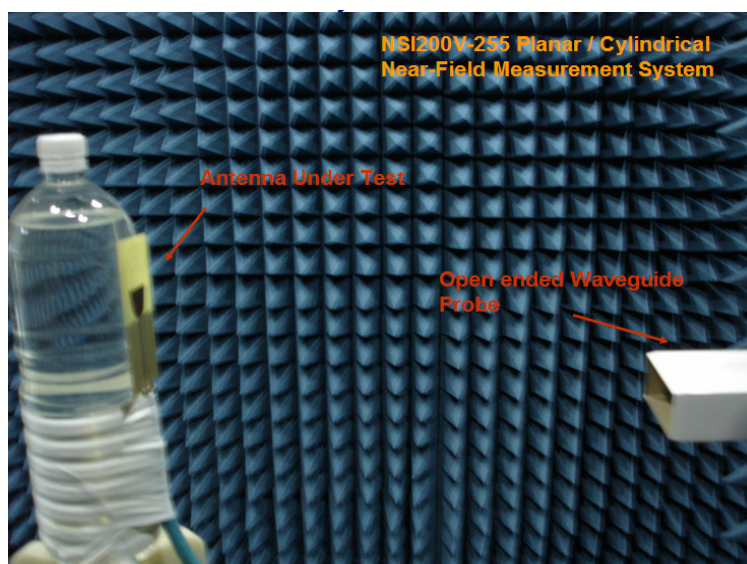
Figure 3.7 A picture of near-field measurement set-up. The distance between the open-ended waveguide probe and the UWB antenna is only 9 cm during the measurement.

(a)

(b)

(c)
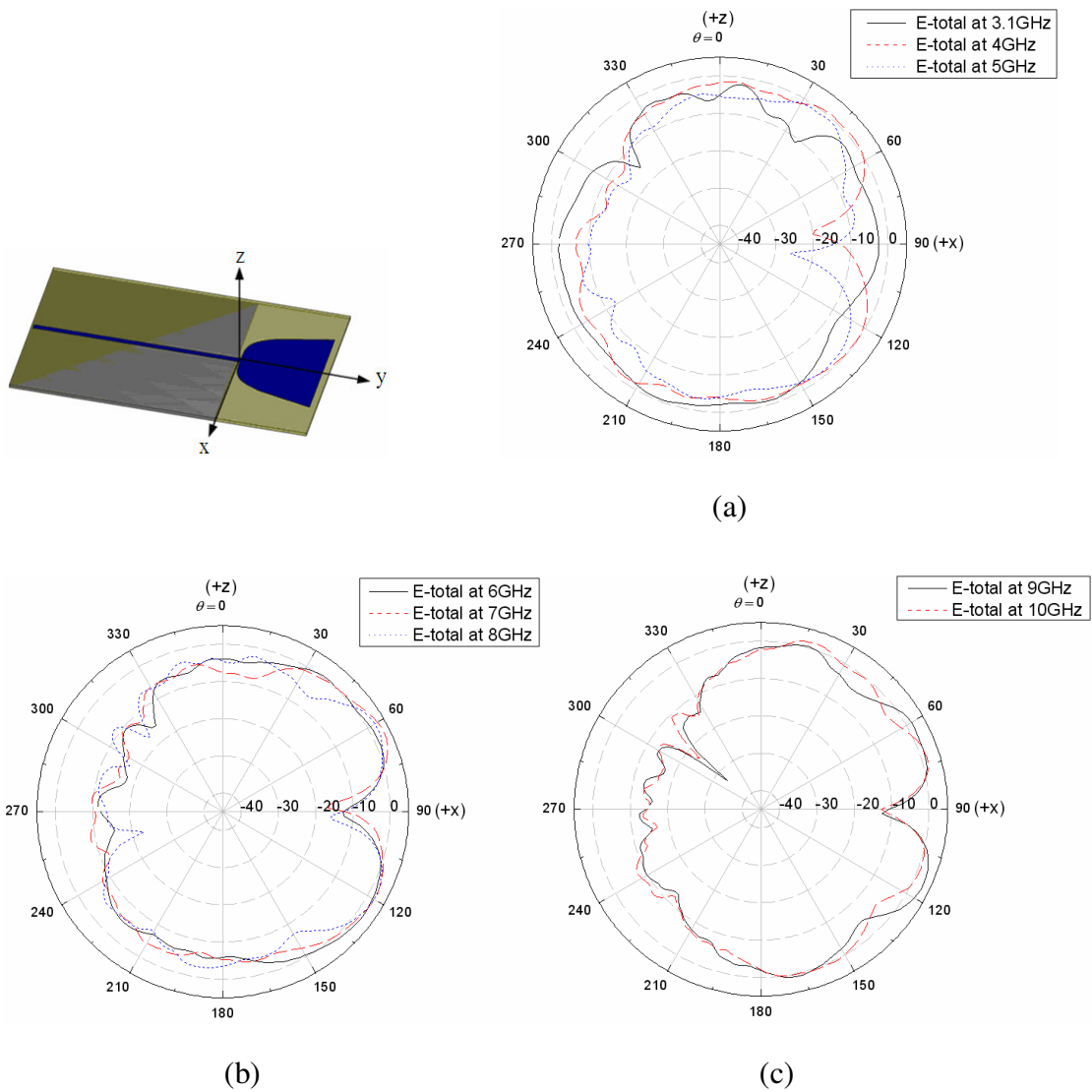
Figure 3.8 Measured far-field radiation pattern of the antenna attached to a bottle of normal saline in the x-z plane (a) E-total at 3.1, 4 and 5GHz (b) E-total at 6, 7 and 8 GHz (c) E-total at 9 and 10 GHz.

(a)

(b)

(c)
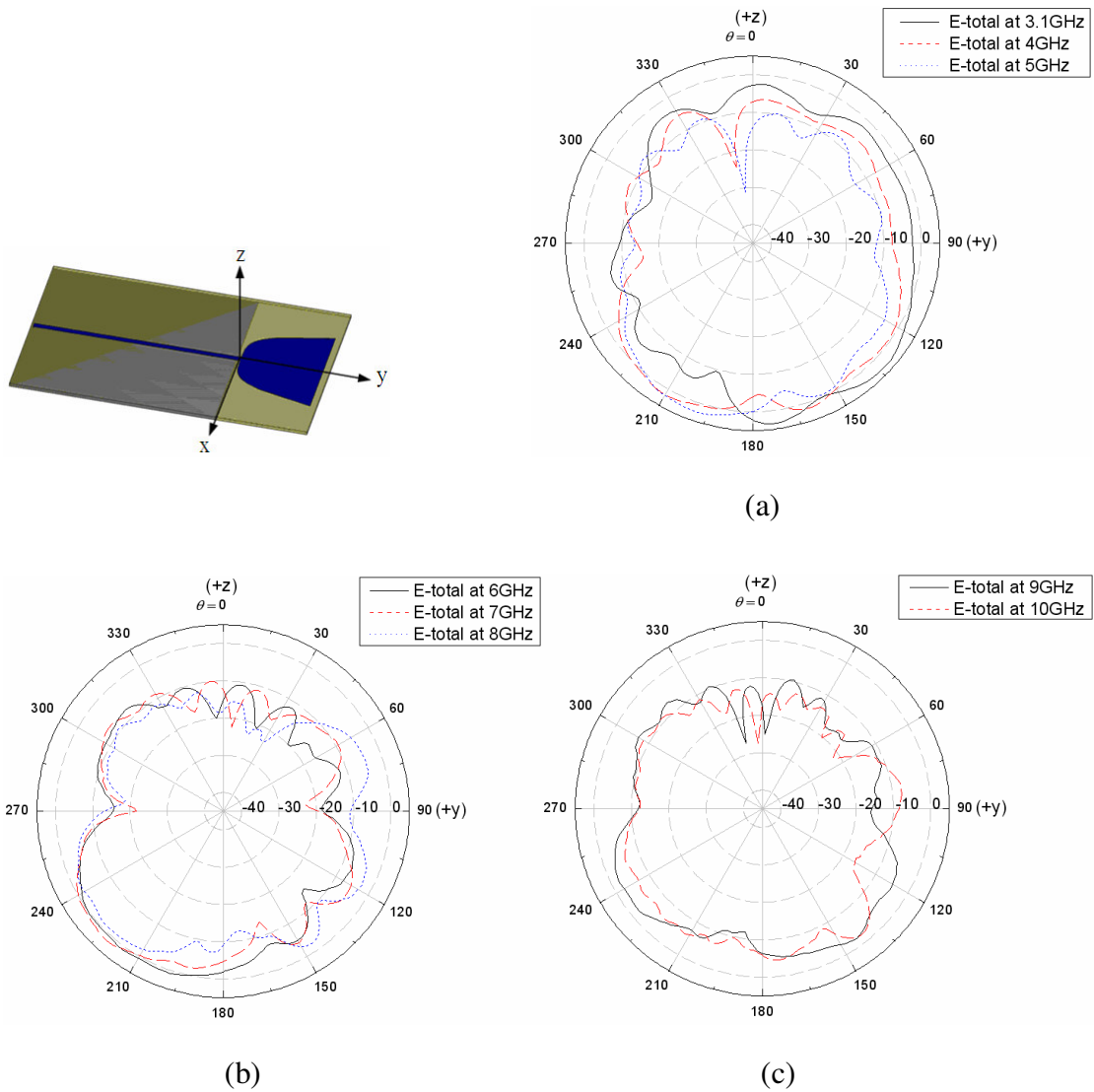
Figure 3.9 Measured far-field radiation pattern of the antenna attached to a bottle of normal saline in the y-z plane (a) E-total at 3.1, 4 and 5 GHz (b) E-total at 6, 7 and 8 GHz (c) E-total at 9 and 10 GHz.

(a)

(b)

(c)
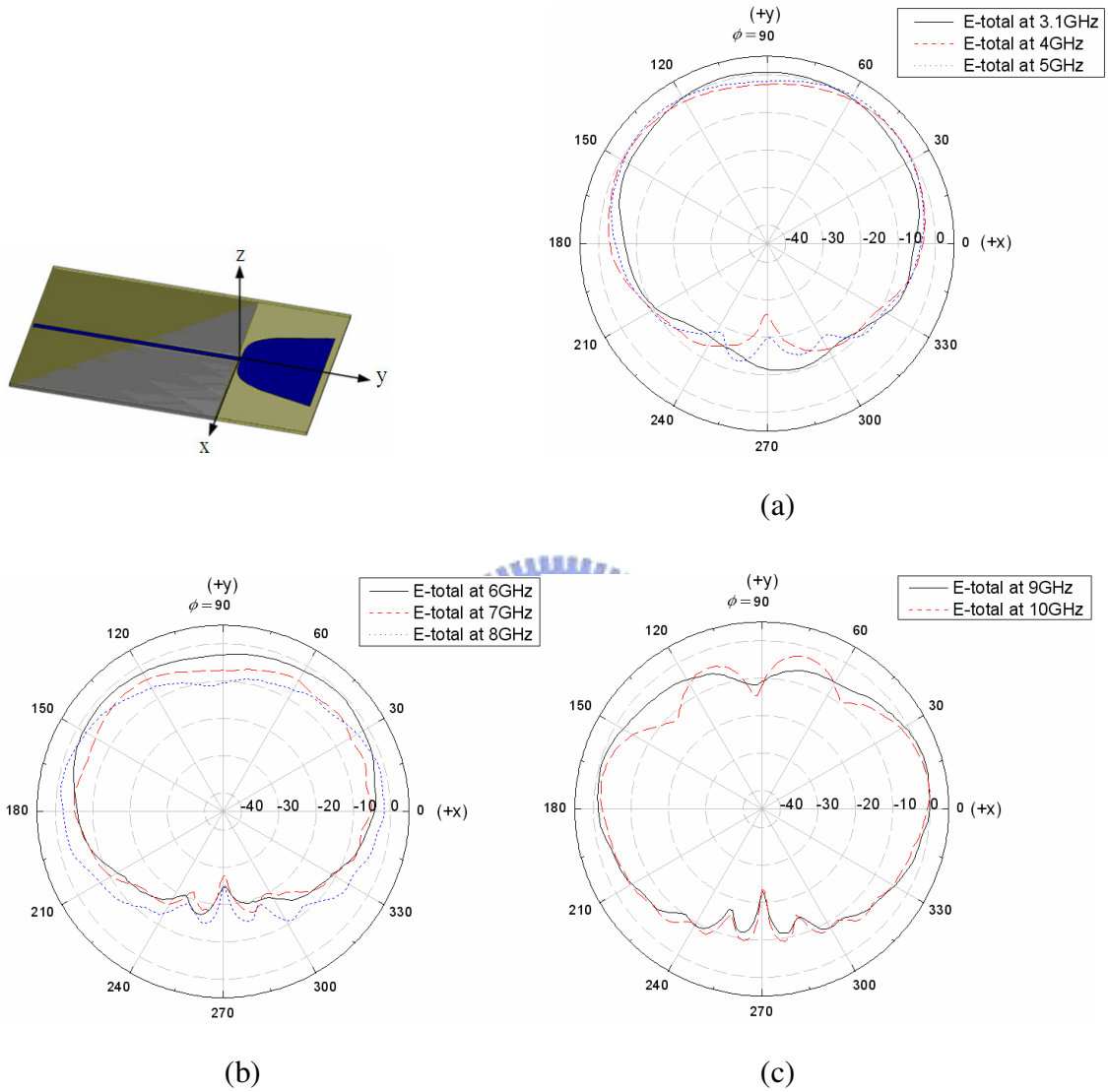
Figure 3.10 Measured far-field radiation pattern of the antenna attached to a bottle of normal saline in the x-y plane (a) E-total at 3.1, 4 and 5 GHz (b) E-total at 6, 7 and 8 GHz (c) E-total at 9 and 10 GHz.
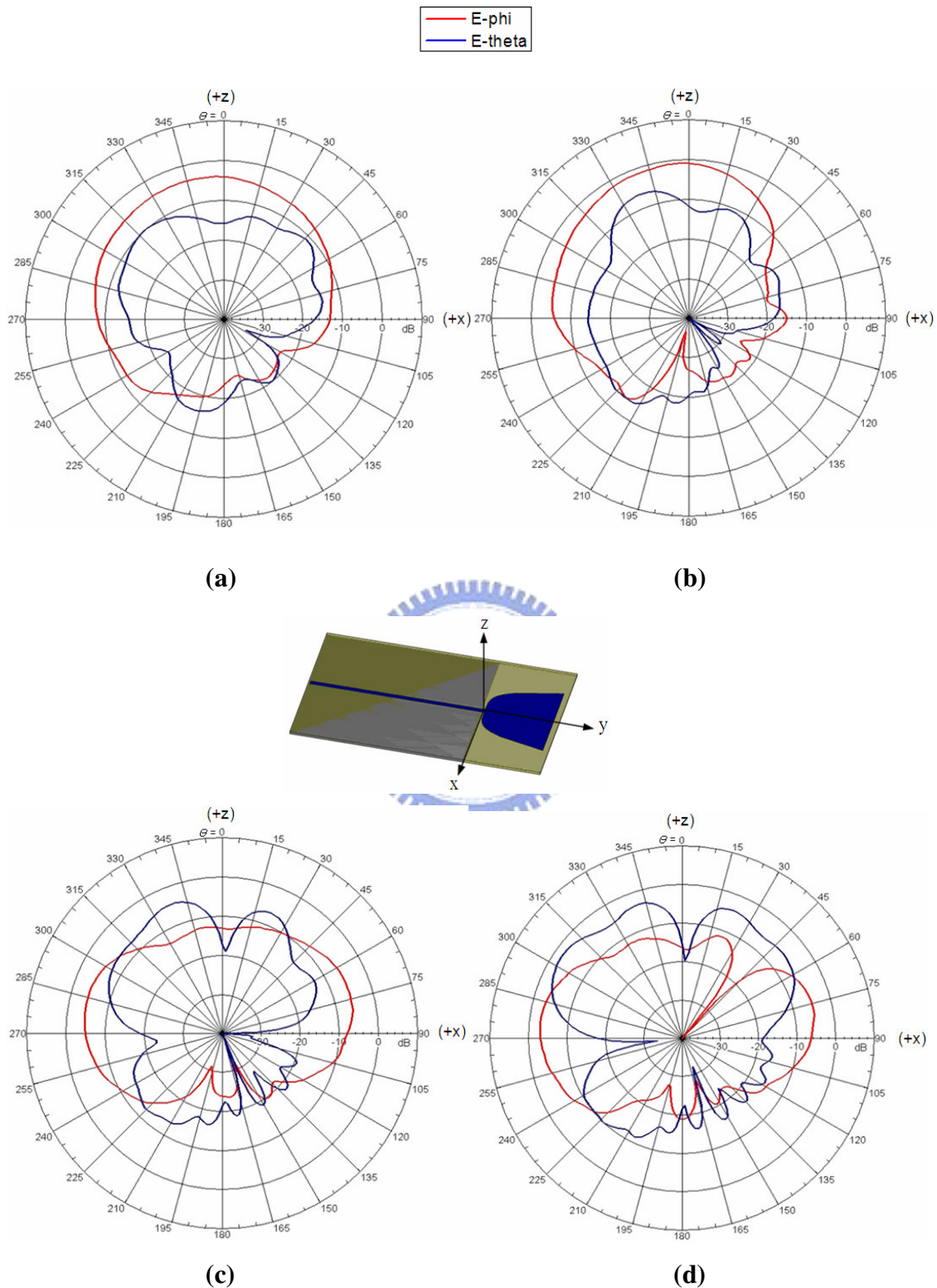
Figure 3.11 Measured near-field pattern of the antenna attached to a bottle of normal saline at (a) 3 GHz, (b) 8 GHz, (c)9 GHz, and (d) 10GHz.

3.2 BAN Channel Measurement System

The system diagram of the BAN channel measurement system is shown in Figure 3.12. One pairs of UWB antennas and an 8719ET vector network analyzer (VNA) composing the measurement system described in Figure 3.13. VNA measures the channel frequency response (S21 parameter) between two antennas in the range 3.1GHz-10GHz. The two antennas are connected to the VNA using 4 meter low-loss coaxial cables. The VNA measures the magnitude and phase of each frequency components allowing the ease of obtaining time domain response by Inverse Discrete Fourier Transform (IDFT).
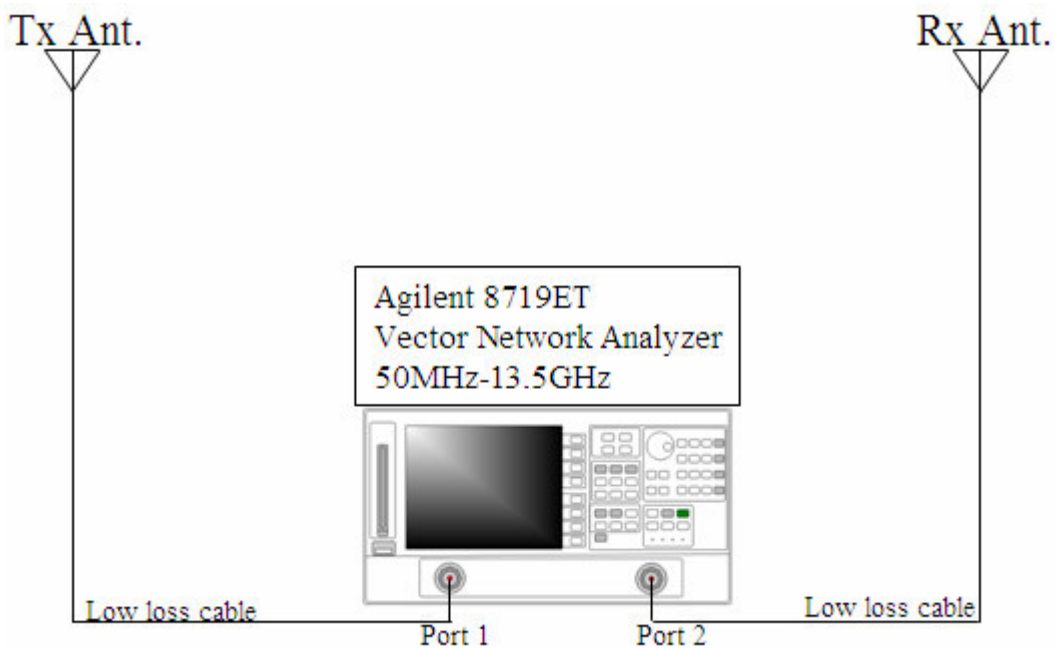
Figure 3.12 System diagram of the measurement system.
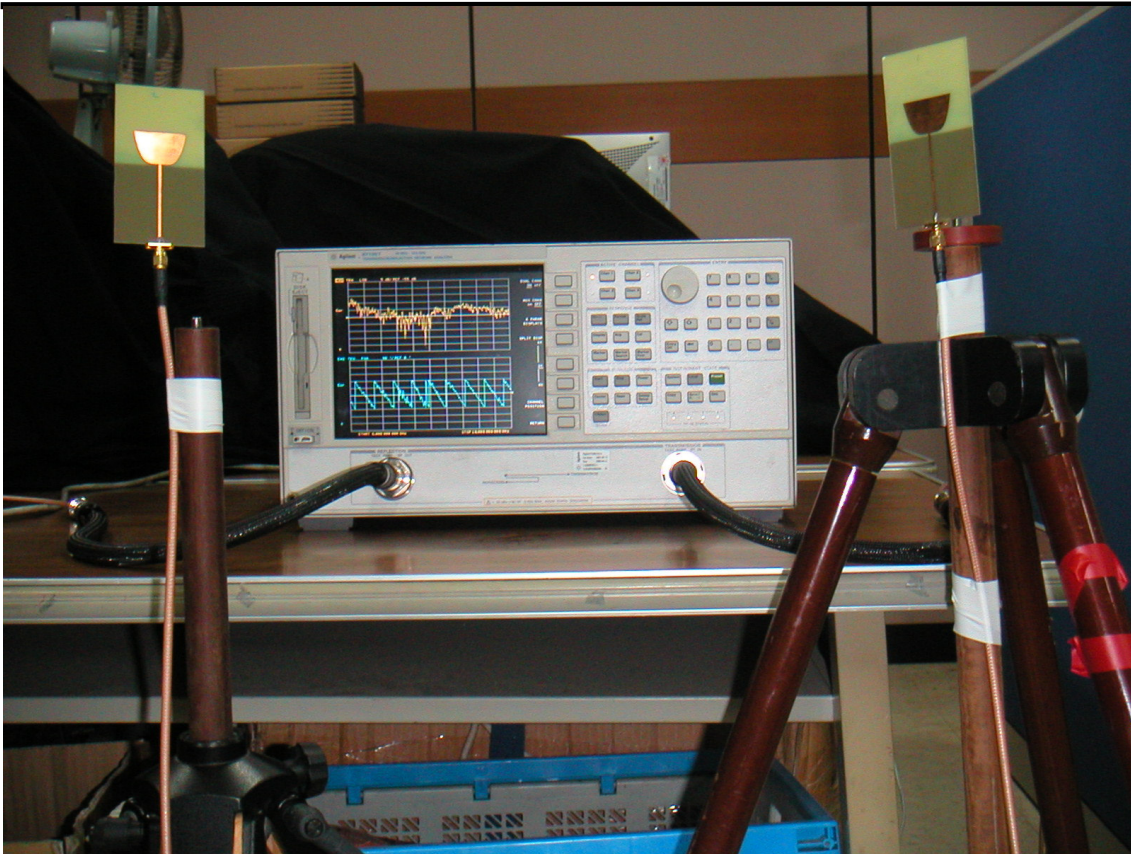
Figure 3.13 A picture of the measurement system.

The power delay profile (PDP) represents the amount of energy collected at the receiver (Rx) of a multi-path channel and the delays associated with this reception. Figures 3.14 and 3.15 illustrate the PDPs of the base-line test, which is done in an anechoic chamber, with Tx-Rx distance equal 20 cm and 50 cm, respectively. In the both figures, the estimated distances are fit in with true distance, a little error caused by the time resolution of frequency bandwidth. Table 3.1 illustrates the true and estimated distance for Figure 3.14 and 3.15

According to above data measured in a chamber, it seems that the noise level of the measurement system is about -80 dB.

(a)

(b)   **(c)**
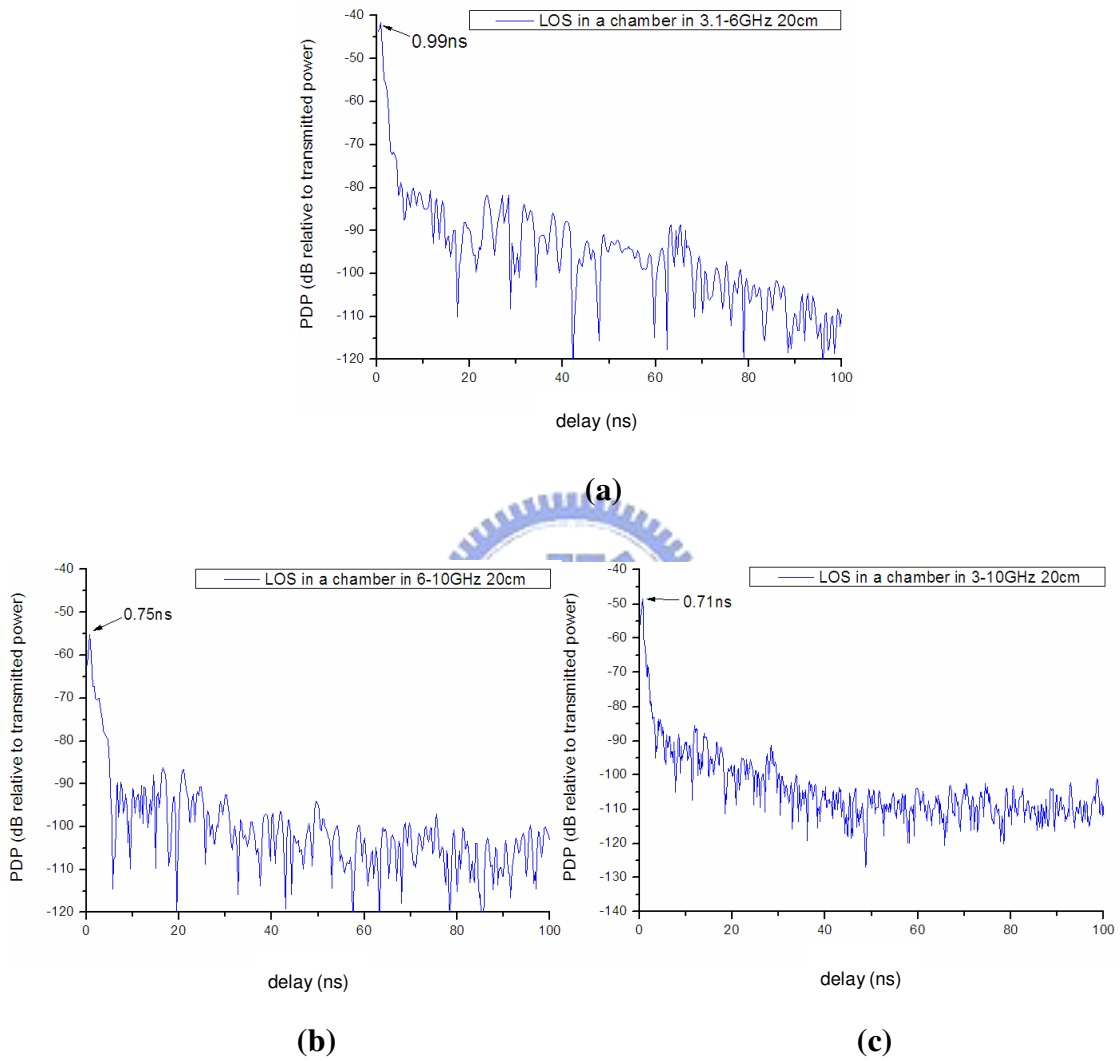
Figure 3.14 PDP for Tx-Rx distance equal to 20cm at (a) 3.1-6, (b) 6-10, (c) 3.1-10 GHz.

(a)

(b)

(c)
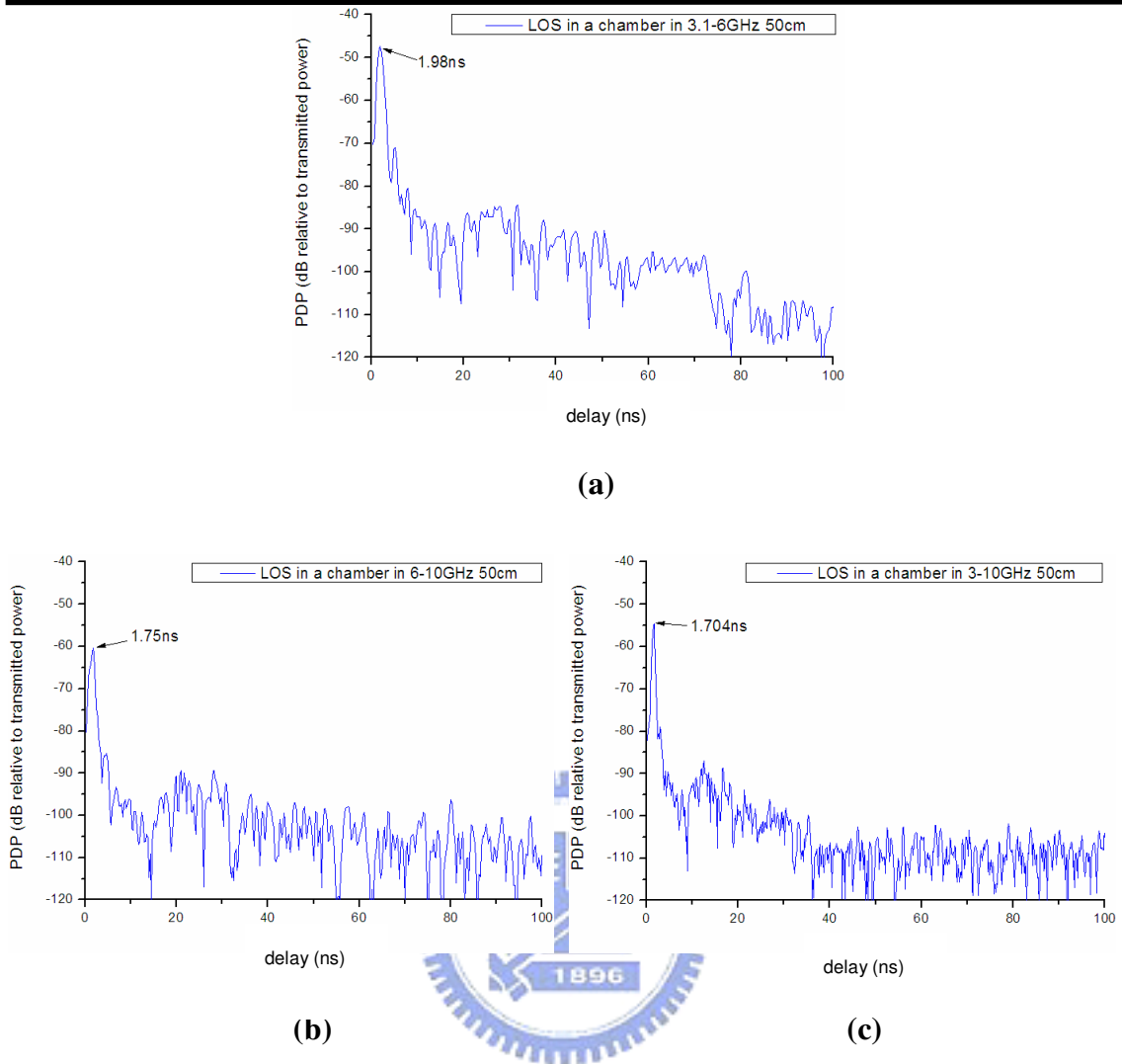
Figure 3.15 PDP for Tx-Rx distance equal to 50cm at (a) 3.1-6, (b) 6-10, (c) 3.1-10 GHz.

Table 3.1 The true and estimated distance for Figure 3.14 and Figure 3.15

	Tx-Rx distance (cm)	Delay time of the directed wave (ns)	Estimated Tx-Rx distance (cm)
Figure 3.14 (a)	20	0.99	29.7
Figure 3.14 (b)	20	0.75	22.5
Figure 3.14 (c)	20	0.71	21.3
Figure 3.15 (a)	50	1.98	59.4
Figure 3.15 (b)	50	1.75	52.5
Figure 3.15 (c)	50	1.704	51.12

3.3 Measurement Setup for BANs

3.3.1 Setup for SISO measurement

Figure 3.16 shows the setup for measurements near the body. In all cases, the body is in a standing position with arms hanging along the side. The Agilent 8719ET VNA measures S21 parameter between two antennas attached on the body. The two antennas are connected to the VNA using low-loss coaxial cables. The antennas are mounted on the body as shown in Figure 3.17. The Rx positions are marked with white circles, while the transmitter (Tx) position is marked with black circle. The Tx is always placed on the front of the body, and the Rx is placed at various positions on the body. Figure 3.18 shows where the Tx and Rx are placed on the body. All parameters are extracted from measurements performed in six planes separated by 5cm along the z axis of the body. Figure 3.19 shows where the antennas are placed on the body for each plane.
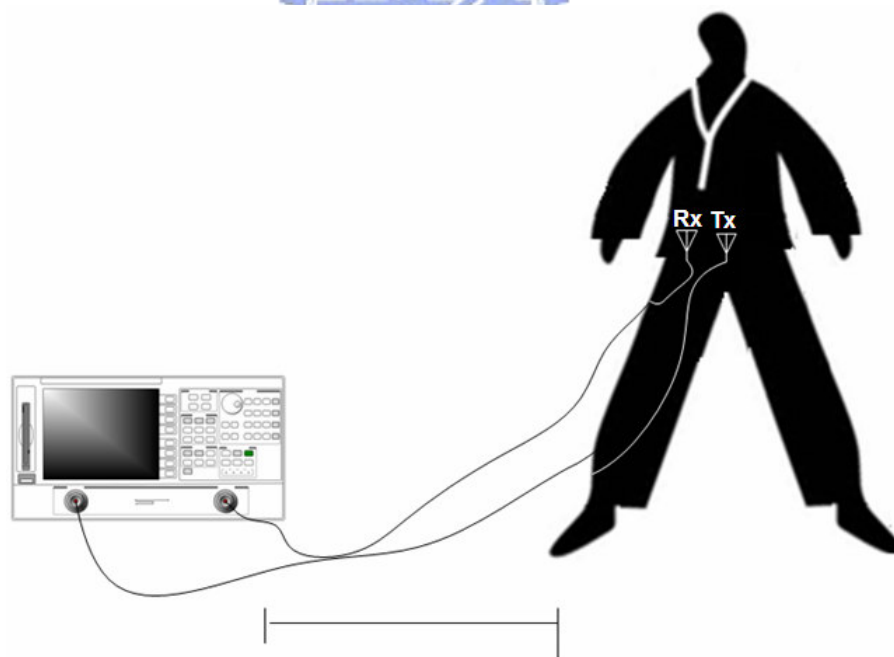
Figure 3.16 Setup of UWB channel measurement.
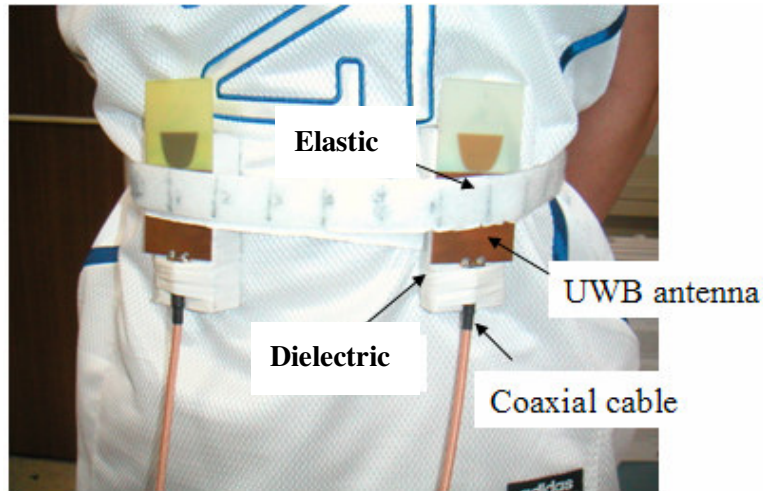
Figure 3.17 The UWB antennas mounted on the body.

● : the position of Tx antenna
○ : the position of Rx antenna
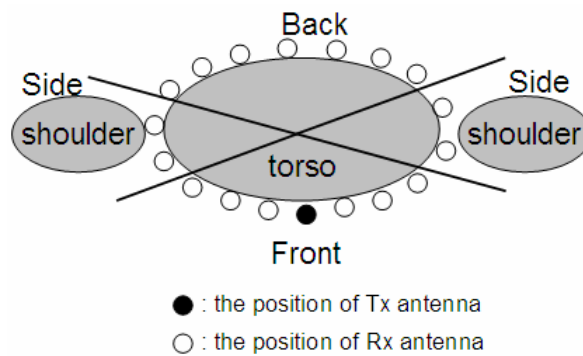
Figure 3.18 The locations of Tx and Rx antennas for each body-sector measurement. The Tx antenna is fixed and the Rx antenna is moving around the body during the measurement.

6 planes
5cm

110cm
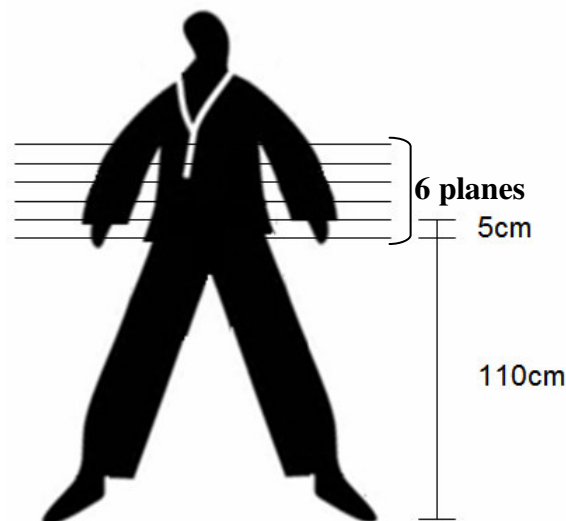
Figure 3.19 Six body –sector measurements are done. Neighboring cross-planes are separated by 5 cm.

3.3.2 Setup for MIMO measurement

With a SISO system, we have simulated a 5×5 MIMO channels around the body by moving the Tx and Rx antennas to the ULA (uniform Linear Array) fixed point, the space of antennas elements is 3 cm. Figure 3.20 shows where the Tx and Rx are placed on each body-sector. The Tx elements are always placed on the front of the body, and the Rx elements are placed at four positions such as MIMO_1, MIMO_2, MIMO_3 and MIMO_4 on the body. Table 3.2 lists the main parameter in the SISO and MIMO measurement.
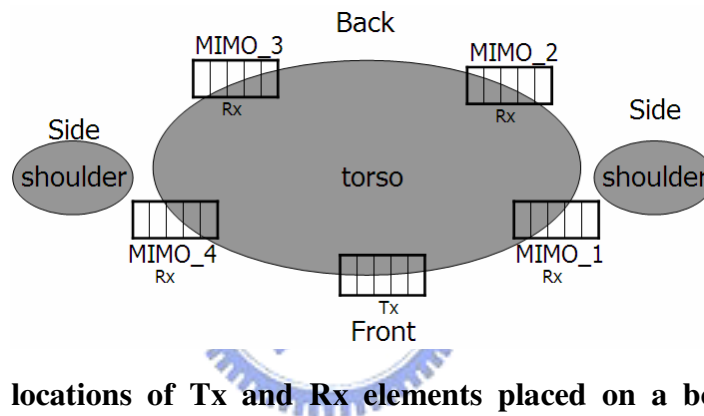
Figure 3.20 The locations of Tx and Rx elements placed on a body-sector for MIMO measurement.

Table 3.2 Main parameters in the measurement

Parameter	Value
Frequency band	3.1-10GHz、3.1-6GHz、6-10GHz
Bandwidth	7GHz、3GHz、4GHz
Number of points over the band	801
Transmitted power	0dBm
Antenna gain	3.49dBi

3.4 Measurement Environment

The measurement was performed at 1st (sites A and B) and for the LOS tests , 2nd (site C and D) for BANs and 8th for both LOS and BANs of the Microelectronic and Information System Research Center (MISRC) at the National Chiao-Tung University, Hsinchu, Taiwan. The floor layouts of these measurement sites are shown in Figure 3.21
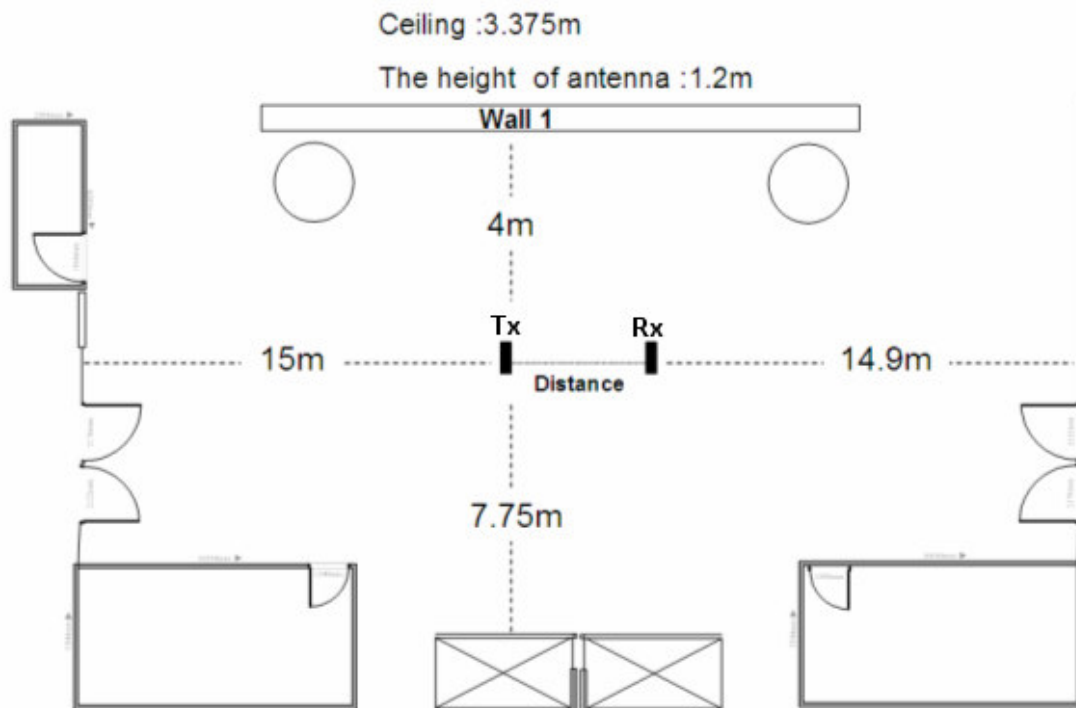
Figure 3.21 (a) Floor layout of site A (LOS without nearby local scatterers), which is located at 1st floor of MISRC.
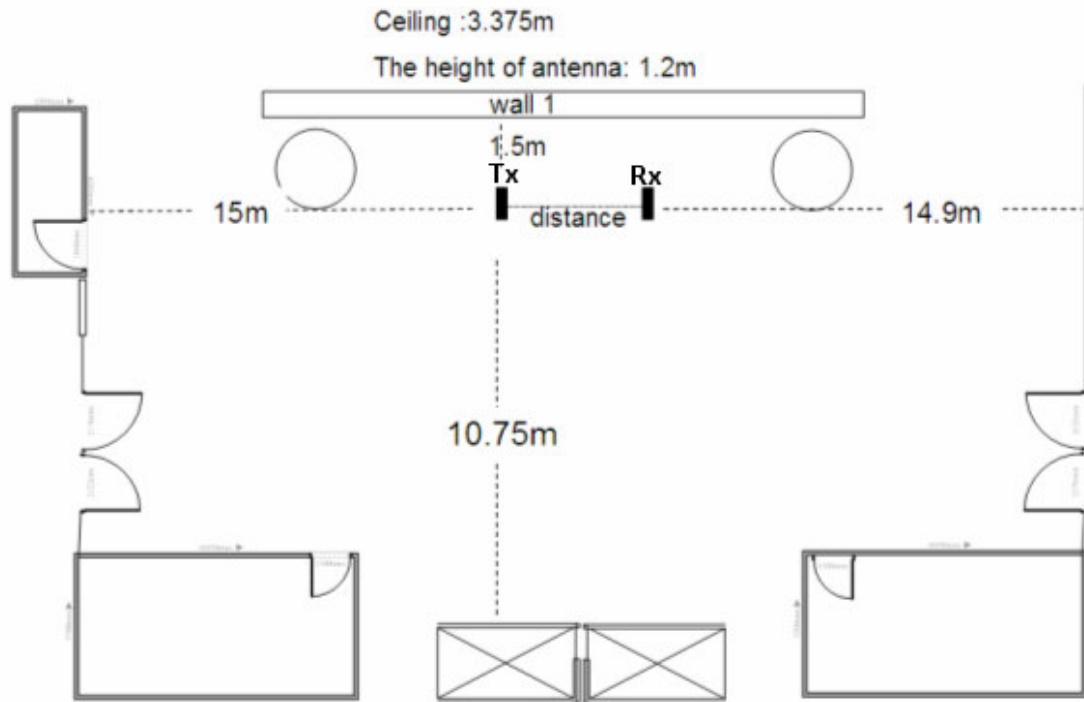
Figure 3.21 (b) Floor layout of site B (LOS near a wall, the distance between the direct path and wall 1 is 1.5m), which is located at 1st floor of MISRC.
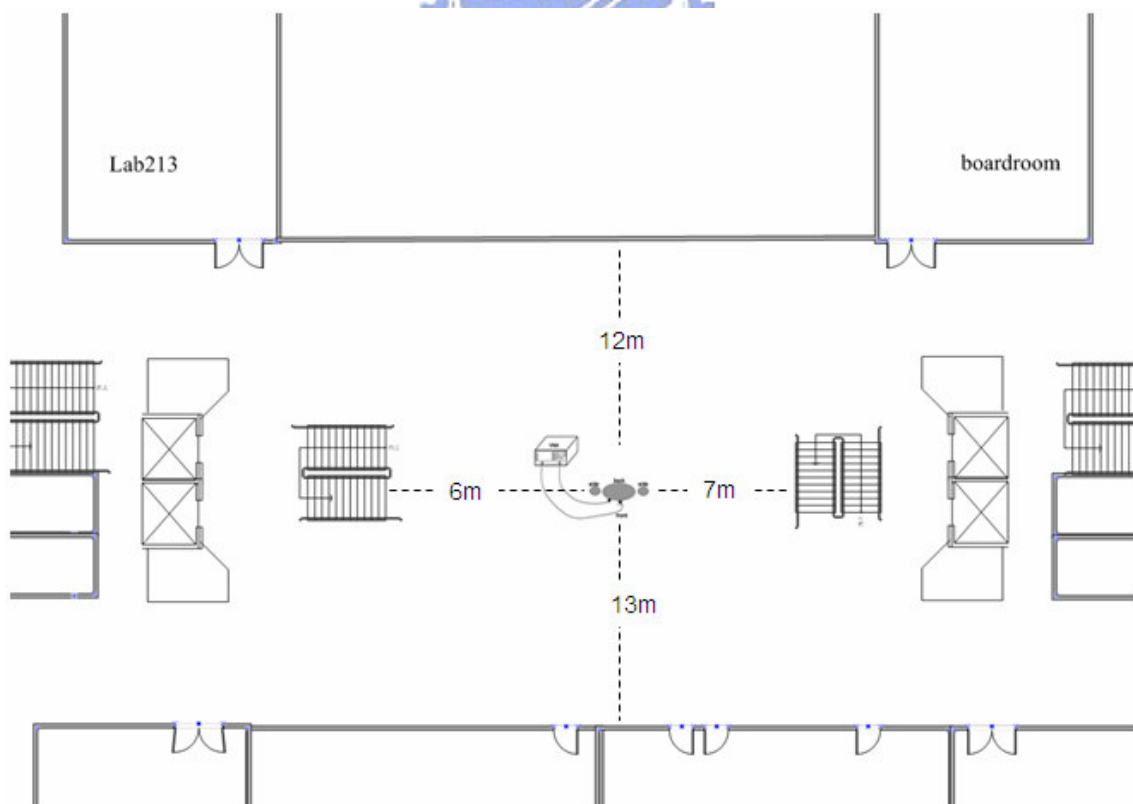
Figure 3.21 (c) Floor layout of site C (without local scatterers), which is located at 2nd floor of MISRC.
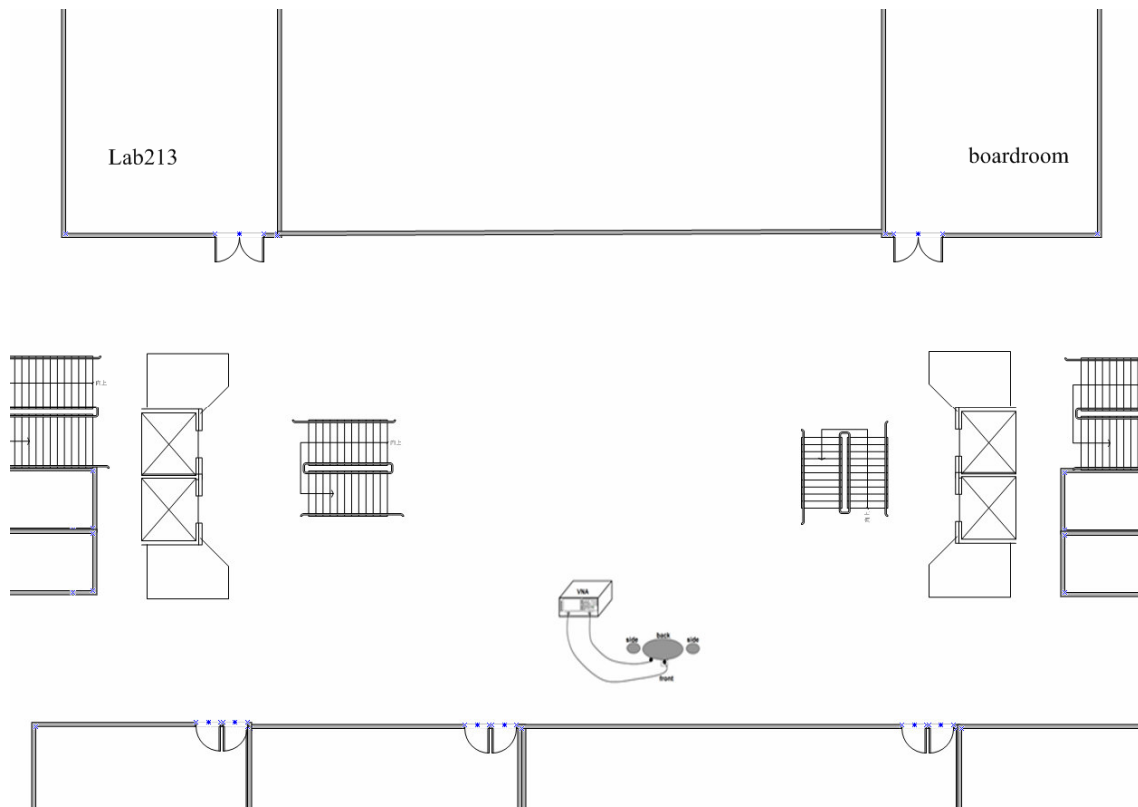
Figure 3.21 (d) Floor layout of site D (near a wall), which is located at 2nd floor of MISRC.
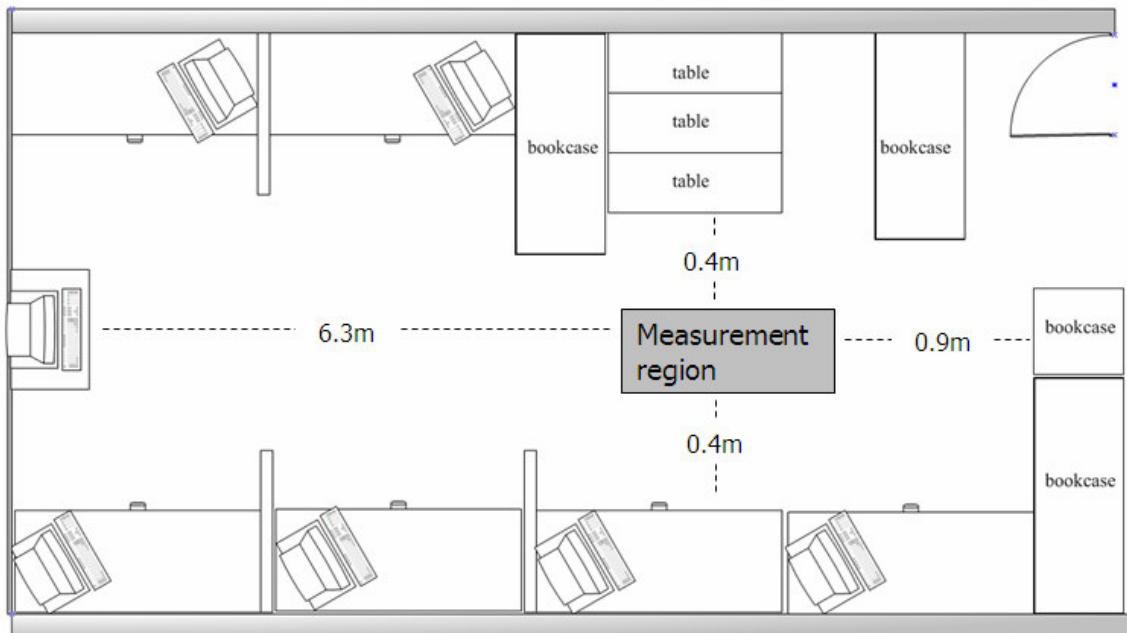
Figure 3.21 (e) Floor layout of site E (with dense local scatterers), which is located at Lab 810 of the 8th floor of MISRC.

3.5 The LOS Measurement for UWB Radio Channels (Without Body Effect)

In order to know the UWB BAN radio channel measurement system is correctly, we measured the LOS situation at site A, B and E. In a typical indoor environment, due to reflection, diffraction and scattering of radio waves by structures inside a building, the transmitted signal most often reaches the Rx by more than one path, resulting in a phenomenon known as multipath fading. The propagation path is classified due to different mechanisms:

Cat. I : directed path

Cat. II : path due to ground reflection

Cat. III: path due to ceiling reflection

Cat. IV: path due to wall reflection

Cat. V : multipath cluster due to scattering
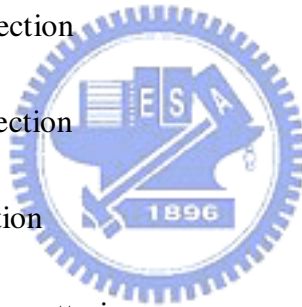
3.5.1 The Measurement Result at Site A and Site B

We can know where the multipath reflected from obviously, if we convert the arrived time of the effective signal path to estimated distance. There are no local scatterers around the antennas at site A, therefore, except the directed wave (I), there are ground (II) and ceiling reflection(III) shown in Figures 3.22 and 3.23 (a), (c) and (e). At site B, the measurement scenario is near a wall and no other scatterers. The wall reflection (IV) would be observed in Figures 3.22 and 3.23 (b), (d) and (f). Table 3.3 illustrates the true and estimated distance of Figure 3.22 and Figure 3.23. The error of

true and estimate distance is no more than 18 cm.

(a)

(b)

(c)

(d)

(e)

(f)
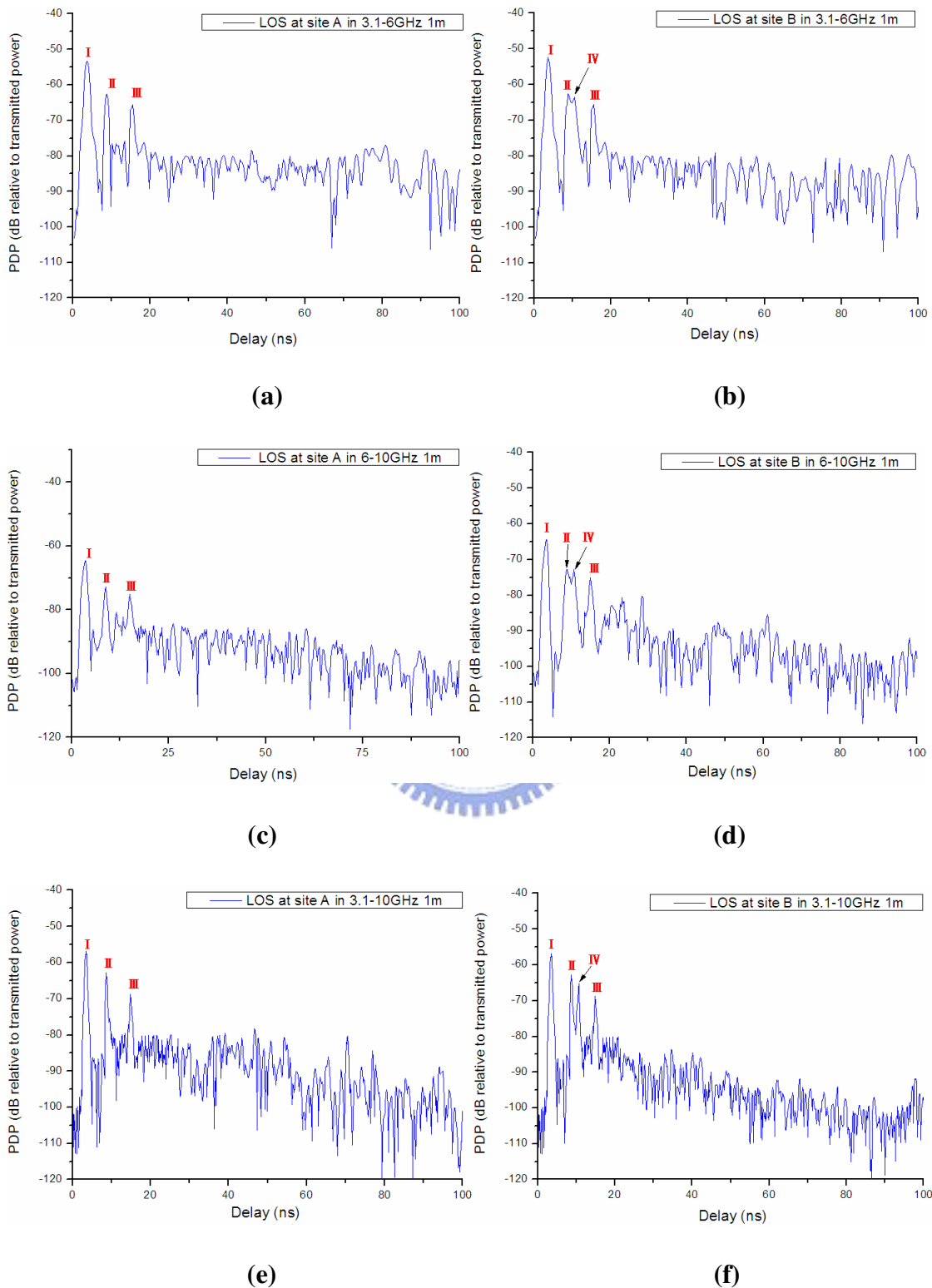
Figure 3.22 PDP for Tx-Rx distance is equal to 1m at

(a) site A, at 3.1 – 6 GHz,   (b) site B, at 3.1 – 6 GHz,

(c) site A, at 6 – 10GHz,   (d) site B, at 6 – 10GHz,

(e) site A, at 3.1 – 10 GHz   (f) site B, at 3.1 – 10 GHz

(a)

(b)

(c)

(d)

(e)

(f)
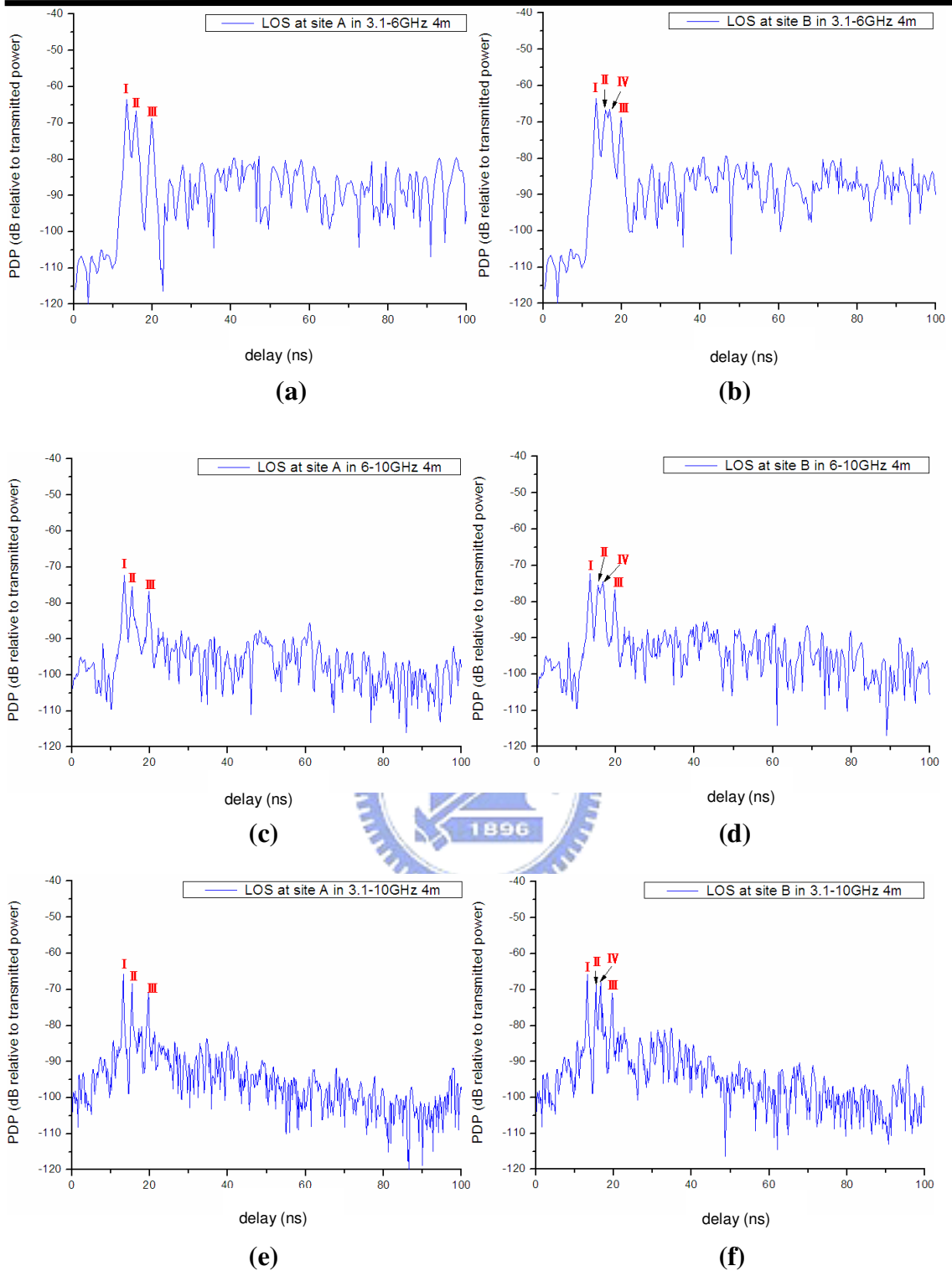
Figure 3.23 PDP for Tx-Rx distance is equal to 4m at

(a) site A, at 3.1 – 6 GHz,   (b) site B, at 3.1 – 6 GHz,

(c) site A, at 6 – 10GHz,   (d) site B, at 6 – 10GHz,

(e) site A, at 3.1 – 10 GHz   (f) site B, at 3.1 – 10 GHz

Table 3.3 The true and estimated distances of Figure 3.22

	True distance (m)				Estimated distance (m)			
	I	II	III	IV	I	II	III	IV
Figure 3.22(a)	1	2.45	4.37	-	1.09	2.69	4.55	-
Figure 3.22 (b)	1	2.6	4.46	3.16	1.09	2.67	4.55	3.17
Figure 3.22 (c)	1	2.45	4.37	-	1.05	2.63	4.5	-
Figure 3.22 (d)	1	2.6	4.46	3.16	1.05	2.63	4.5	3.23
Figure 3.22 (e)	1	2.45	4.37	-	1.02	2.64	4.47	-
Figure 3.22 (f)	1	2.6	4.46	3.16	1.02	2.64	4.47	3.2
Figure 3.23(a)	4	4.66	5.9	-	4.06	4.75	5.94	-
Figure 3.23 (b)	4	4.66	5.9	5	4.06	4.75	5.94	5.05
Figure 3.23 (c)	4	4.66	5.9	-	4.05	4.65	5.93	-
Figure 3.23 (d)	4	4.66	5.9	5	4.05	4.72	5.93	5.03
Figure 3.23 (e)	4	4.66	5.9	-	3.96	4.64	5.92	-
Figure 3.23 (f)	4	4.66	5.9	5	4	4.64	5.92	5.03

3.5.2 The Test Result at Site E

The principal purpose is observes the heavy cluster at site C. In addition to the directed wave, ground and ceiling reflection, the multipath components caused by scatterers (Ⅴ) around the antennas can be observed in Figure 3.23.

To making a comprehensive survey of above test data, we can make sure the measurement system is correctly.
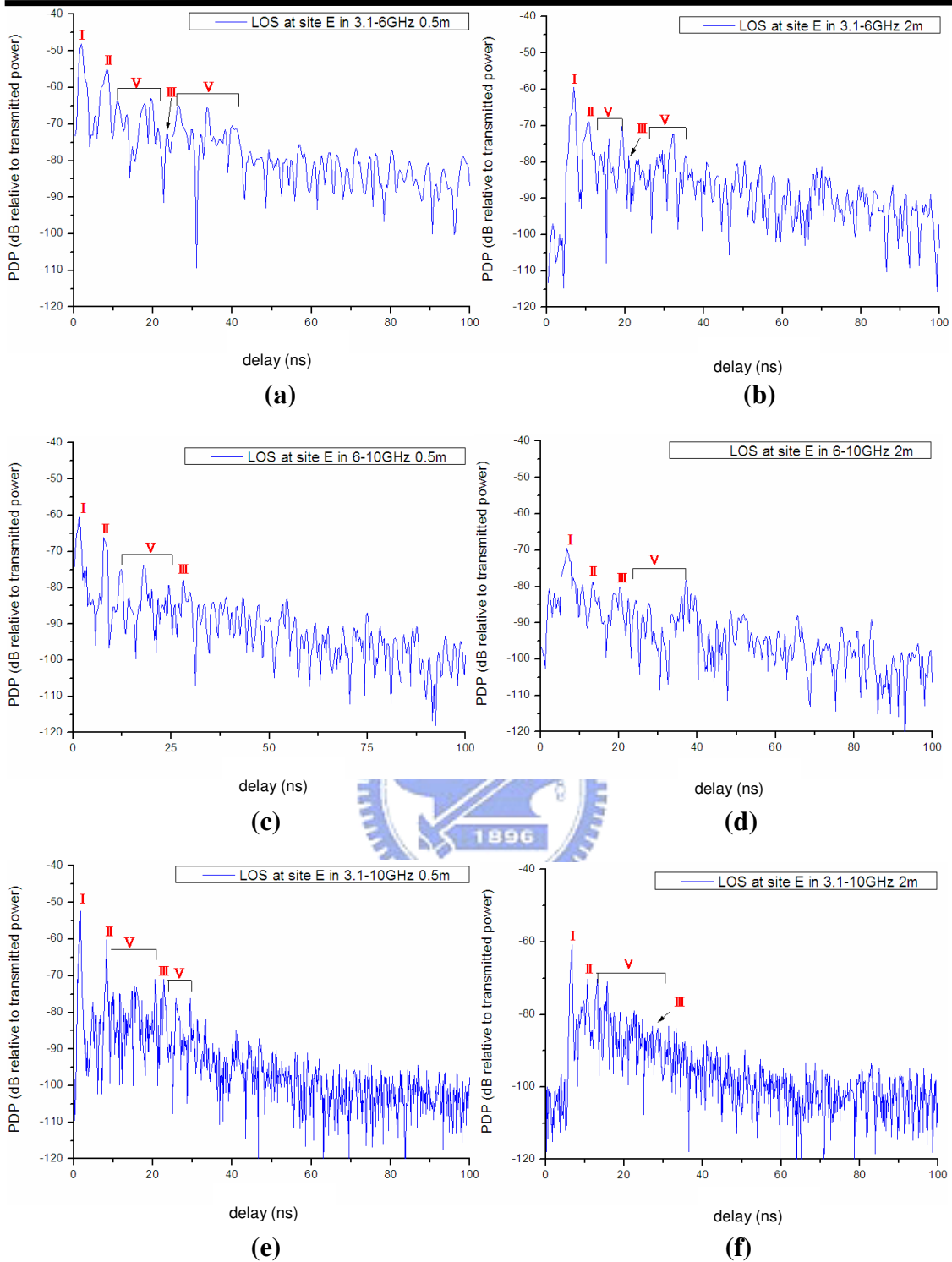
Figure 3.24 PDP for Tx-Rx distance is equal to

(a) 0.5m at 3.1 – 6 GHz, (b) 2m at 3.1 – 6 GHz

(c) 0.5m at 6 – 10 GHz, (d) 2m, at 6 - 10 GHz

(e) 0.5m at 3.1 – 10 GHz, (f) 2m at 3.1 – 10 GHz at site E.

Chapter 4   *Measurement and Modeling of UWB SISO BAN Channel*

4.1 BAN Channel Modeling
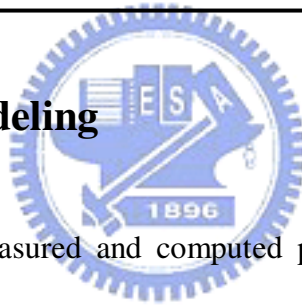
Figure 4.1 shows the measured and computed path losses versus distance. The distance is the wave-traveling distance around the perimeter of the body. The computed result is done by using the path loss model described by

$$PL(d) = PL(d_0) + 10n\log\left(\frac{d}{d_0}\right) \tag{4.1}$$

n: path loss exponent

d_0: reference distance

d: Tx-Rx separation distance

It is found that the measurement results are fitted well by the model as shown in

Figures 4.1, 4.2 and 4.3. The standard deviation, σ ,which is the average variation of the computed and measured data, is no more than 2.7dB. The result is consistent with other research results [3]. Compared with free space (n=2), the path loss exponent near the body at 3.1-10 GHz is much higher (n=5.69). Except the diffracted wave, there is a reflected wave from the ground at site C. This makes the exponent smaller than that of the chamber. The little difference between exponents of site C and site D is because that at site D there is one more reflected wave received. Due to multipath induced by local scatterers, the exponent at site E is smaller than other sites. To summarize, Table 4.1 shows the channel parameter n and prediction accuracy σ with d_0 equals to 0.06m. The path loss in the three frequency bandwidths at the same site has small difference, which may be due to the effect of antenna radiation patterns measured in chapter 3.

(a)

(b)

(c)

(d)
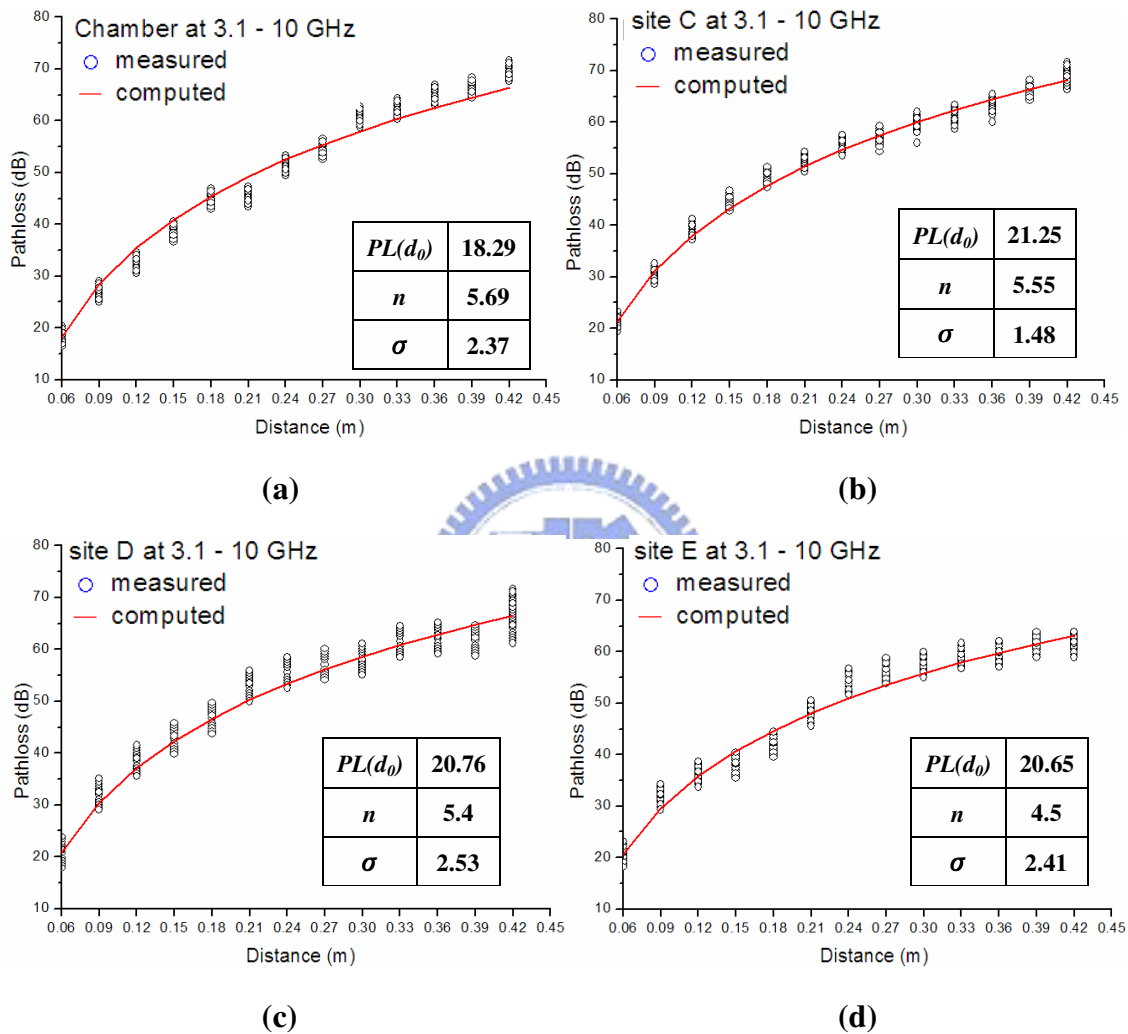
Figure 4.1 Measured and computed 3.1-10 GHz path losses versus the distance around the body, (a) in the chamber, (b) at site C, (c) at site D, (d) at site E.

(a)

(b)

(c)

(d)
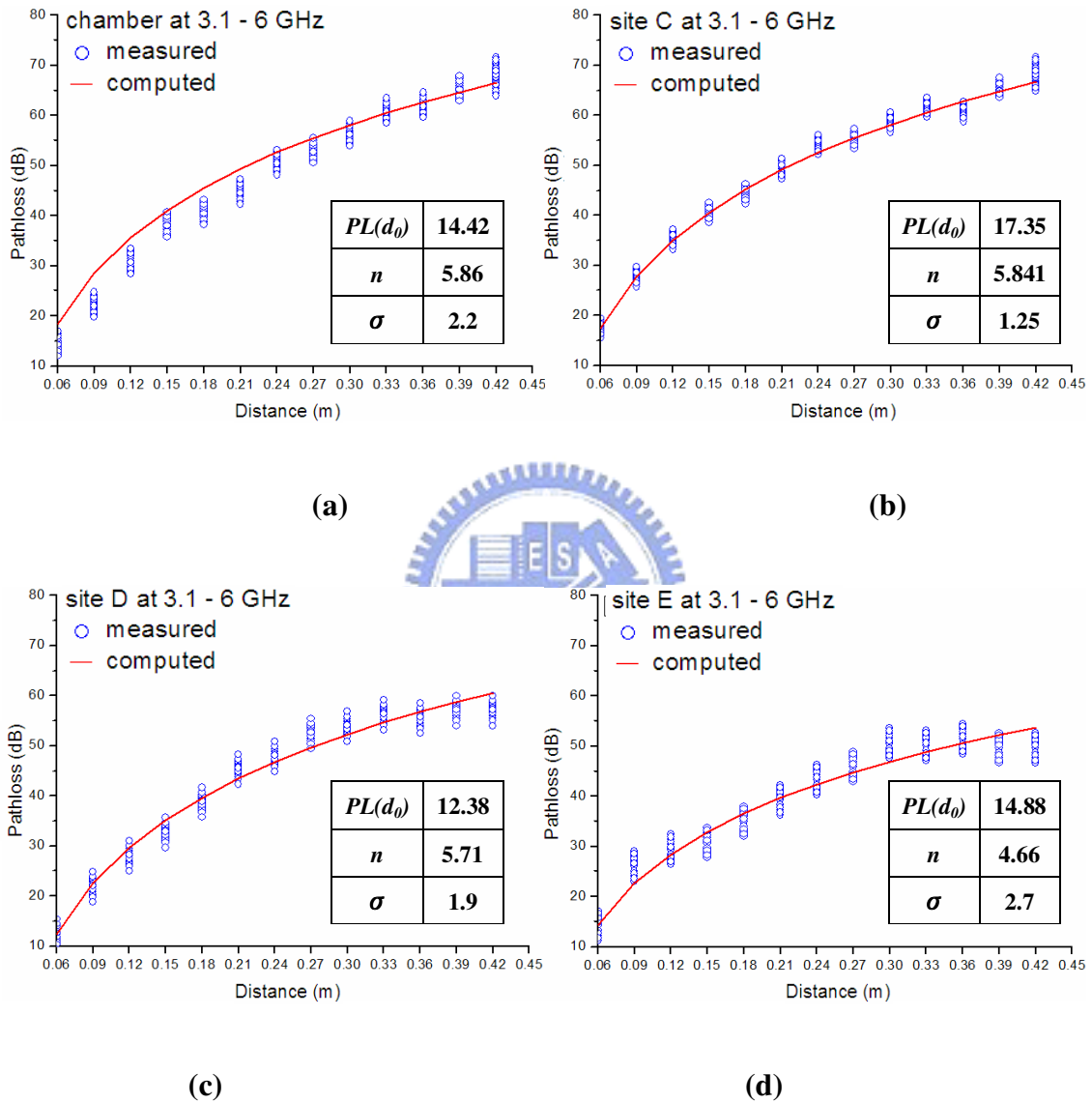
Figure 4.2 Measured path loss around the body (a) in the chamber, at (a) site C, (c) site D, (d) site E at 3.1-6 GHz.

$PL(d_0)$	24.53
n	5.28
σ	2.52

$PL(d_0)$	25.46
n	5.2
σ	1.71

(a)

(b)

$PL(d_0)$	21.34
n	4.93
σ	2.7

$PL(d_0)$	26.04
n	4.4
σ	2.51

(c)

(d)
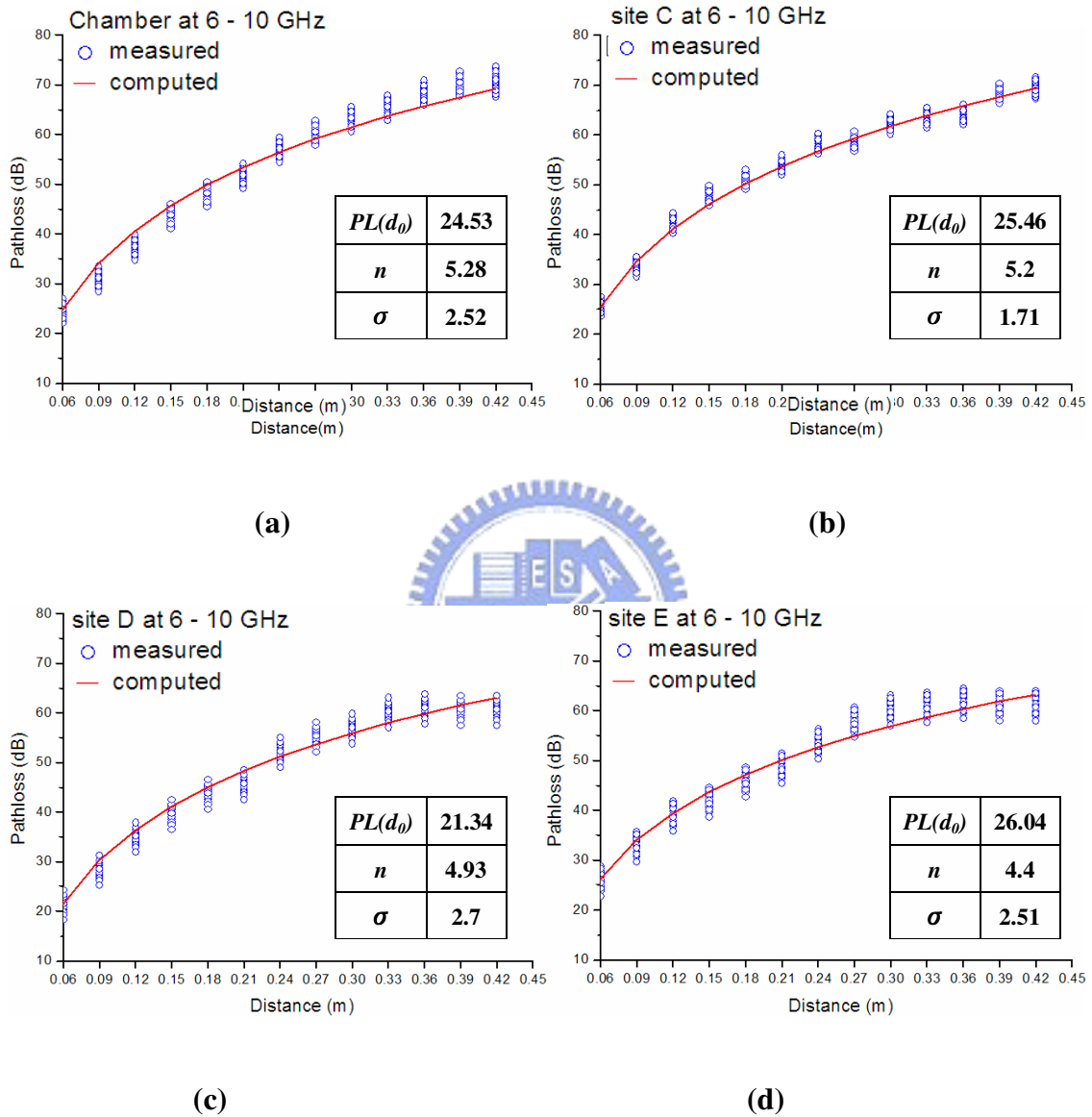
Figure 4.3 Measured path loss around the body (a) in the chamber, at (a) site C, (c) site D, (d) site E at 6-10GHz

Table 4.1 n and σ with d_0 = 0.06m

	3.1-10GHz		3.1-6GHz		6-10GHz	
	n	σ (dB)	n	σ (dB)	n	σ (dB)
Chamber	5.69	2.37	5.86	2.2	5.28	2.52
Site C	5.55	1.48	5.84	1.25	5.2	1.7
Site D	5.4	2.53	5.71	1.9	4.93	2.7
Site E	4.5	2.41	4.66	2.7	4.4	2.51

4.2 Analysis of Measured Temporal Responses

The Averaged Power Delay Profile (APDP) is obtained by averaging a number of PDP of the same excess delay, which is defined by:

$$APDP(t_i) = 1/N \sum_{k=1}^{N} PDP_k(t_i)$$

t_i: i-th time step (sampling point)

N: Number of samples of the same excess delay

The propagation path is classified due to different mechanisms:

Cat.Ⅰ: diffracted path

Cat.Ⅱ: path due to ground reflection

Cat.Ⅲ: path due to wall reflection

Cat.Ⅳ: multipath cluster due to scatterer

4.2.1 Averaged Power Delay Profile Measured in Anechoic Chamber

We measured the radio channel of body area network in an anechoic chamber as base line. There is only a diffracted wave around the body as shown in Figure 4.4. In order to observe the valid signal, the effective range in computing APDP is equal to

20ns. The mean APDP, which is equal to the averaged value of APDP within 20ns, has

shown in Table 4.2.

(a)   (b)   (c)

(d)   (e)   (f)

(g)   (h)   (i)

Figure 4.4 APDP versus delay in the chamber. The receiver placed on the

front of the body at (a)3.1 – 10 GHz, (b)3.1 – 6 GHz, (c)6 – 10 GHz;

side of the body at (d)3.1 – 10 GHz, (e)3.1 – 6 GHz, (f)6 – 10 GHz; and

back of the body at (g)3.1 – 10 GHz, (h)3.1 – 6 GHz, (i)6 – 10 GHz.

Table 4.2 Mean of APDP in the anechoic chamber

μ_{dB} Receiver Position	3.1-10GHz	3.1-6 GHz	6-10 GHz
front	-27.40	-23.47	-33.56
side	-63.53	-62.03	-66.41
back	-81.64	-77.79	-83.51

4.2.2 Averaged Power Delay Profile Measured at Site C

The site C is an open space without local scatterers. The diffracted wave around the body and the reflected wave by the ground are observed in the Figure 4.5. When the receiver placed on the back of the body, the reflected wave by the ground would be obstructed by body and can not be found in Figure 4.5(c)(f)(i). Table 4.3 is the mean of APDP from site D.

(a) (b) (c)

(d) (e) (f)

(g) (h) (i)

Figure 4.5 APDP versus delay at site C. The receiver placed on the front of the body at (a)3.1 – 10 GHz, (b)3.1 – 6 GHz, (c)6 – 10 GHz. side of the body at (d)3.1 – 10 GHz, (e)3.1 – 6 GHz, (f)6 – 10 GHz. back of the body at (g)3.1 – 10 GHz, (h)3.1 – 6 GHz, (i)6 – 10 GHz

Table 4.3 Mean of APDP from the site A

μ_{dB} Receiver Position	3.1-10GHz	3.1-6 GHz	6-10 GHz
front	-31.78	-23.74	-36.46
side	-61.52	-56.89	-73.50
back	-80.15	-75.034	-83.1

4.2.3 Averaged Power Delay Profile Measured at Site D

In addition to the diffracted wave and reflected wave of the ground, there is a reflected wave of the wall at site D shown in Figure 4.6(a)(b)(d)(e)(g)(h). The reflected waves of the ground and wall would be obstructed when the receiver placed on the back of the body shown in Figure 4.6(c)(f)(i). Table 4.3 illustrates the mean of APDP from site D.

(a)   (b)   (c)

(d)   (e)   (f)

(d)   (e)   (f)
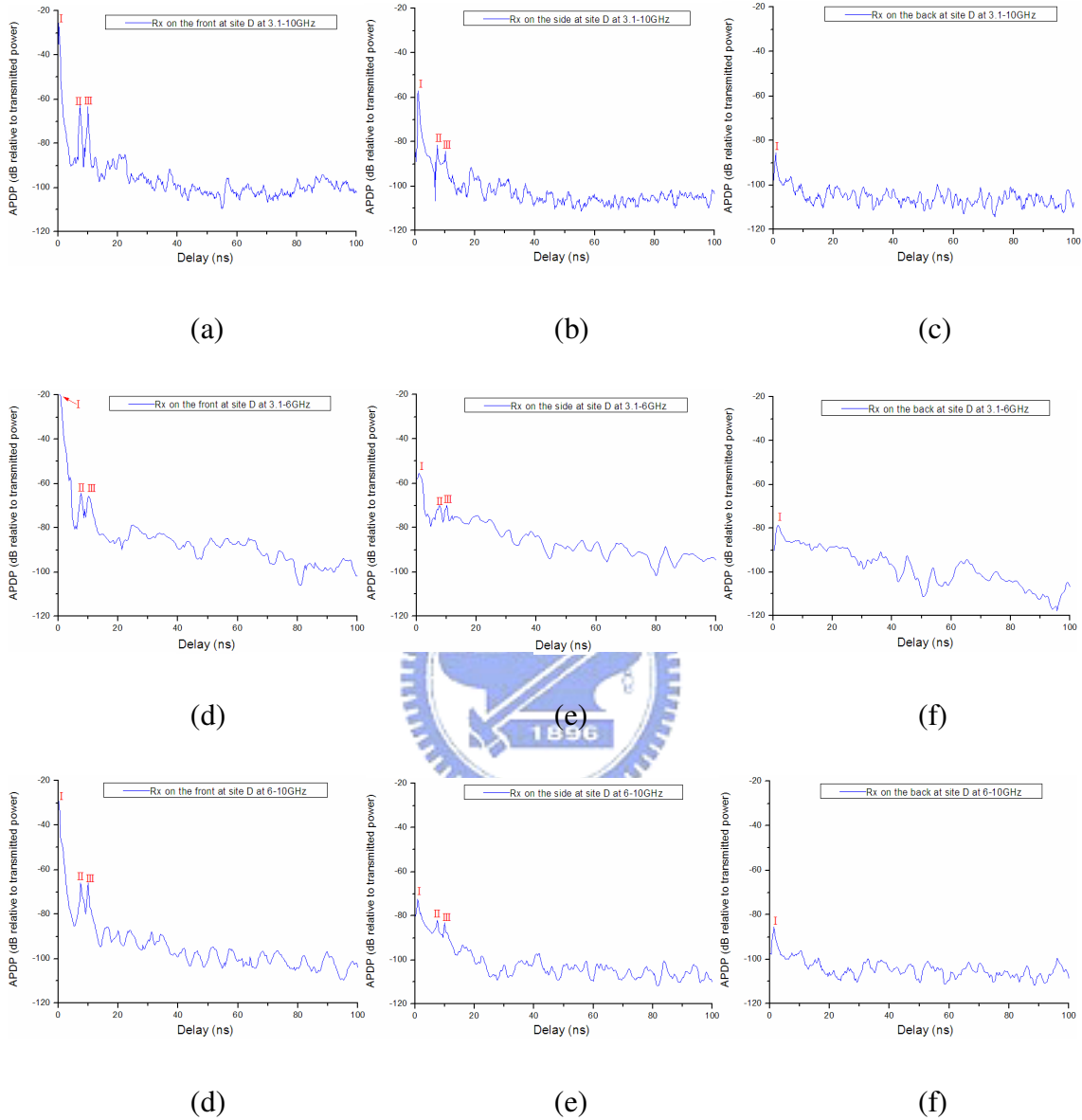
Figure 4.6 APDP versus delay at site D. The receiver placed on the

front of the body at (a)3.1 – 10 GHz, (b)3.1 – 6 GHz, (c)6 – 10 GHz.

side of the body at (d)3.1 – 10 GHz, (e)3.1 – 6 GHz, (f)6 – 10 GHz.

back of the body at (g)3.1 – 10 GHz, (h)3.1 – 6 GHz, (i)6 – 10 GHz

Table 4.3 Mean of APDP from site D

μ_{dB} / Receiver Position	3.1-10GHz	3.1-6 GHz	6-10 GHz
front	-33.48	-25.78	-36.7
side	-63.12	-58.8	-73. 9
back	-85.35	-77.3	-85

4.2.4 Averaged Power Delay Profile Measured at Site E

Site E is differ greatly from other sites with the plenty scatterers around the environment. Figure 4.7 shows the diffracted wave and multipath cluster caused by scatterers. Table 4.4 illustrates the mean of APDP from site E.
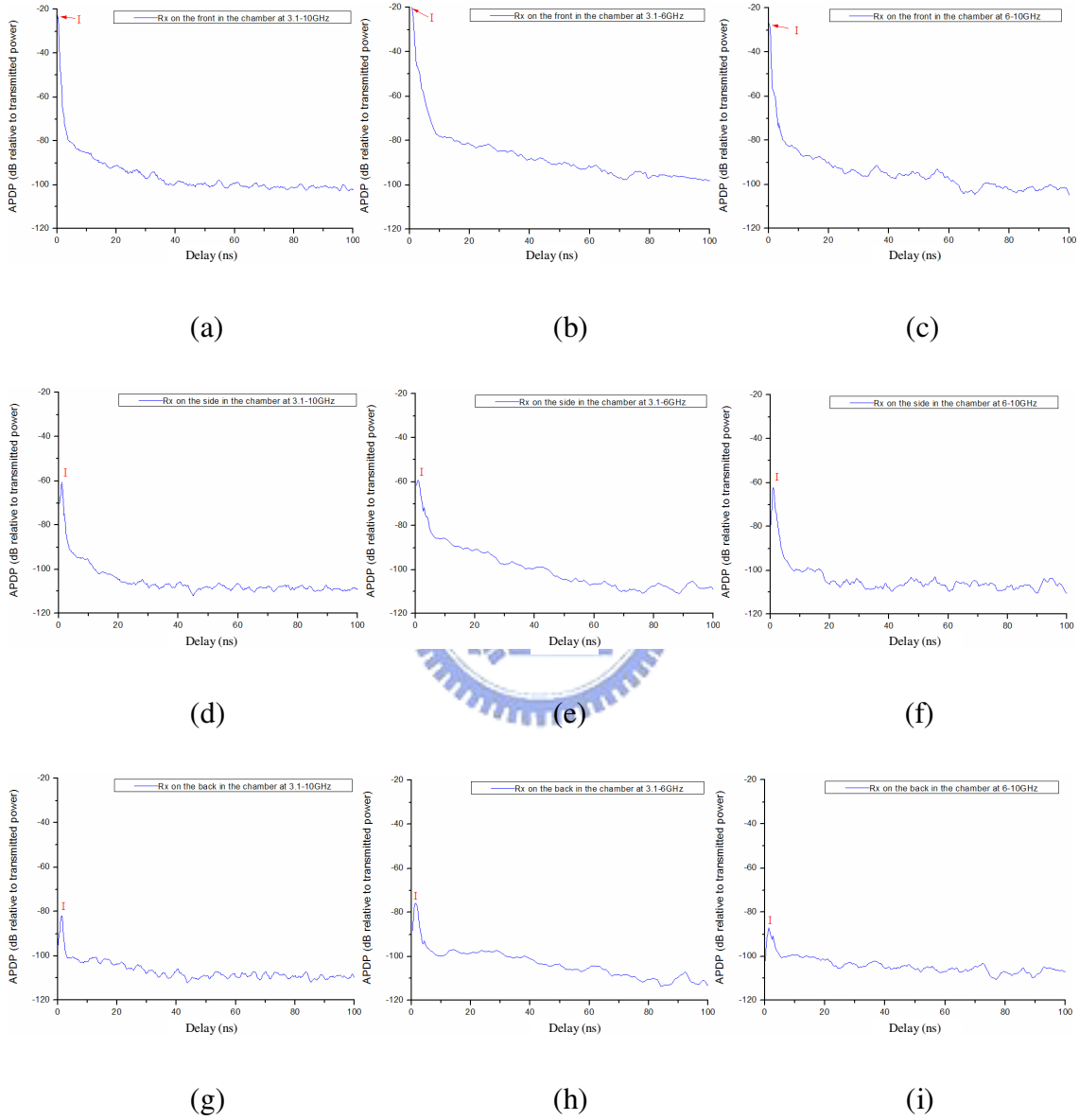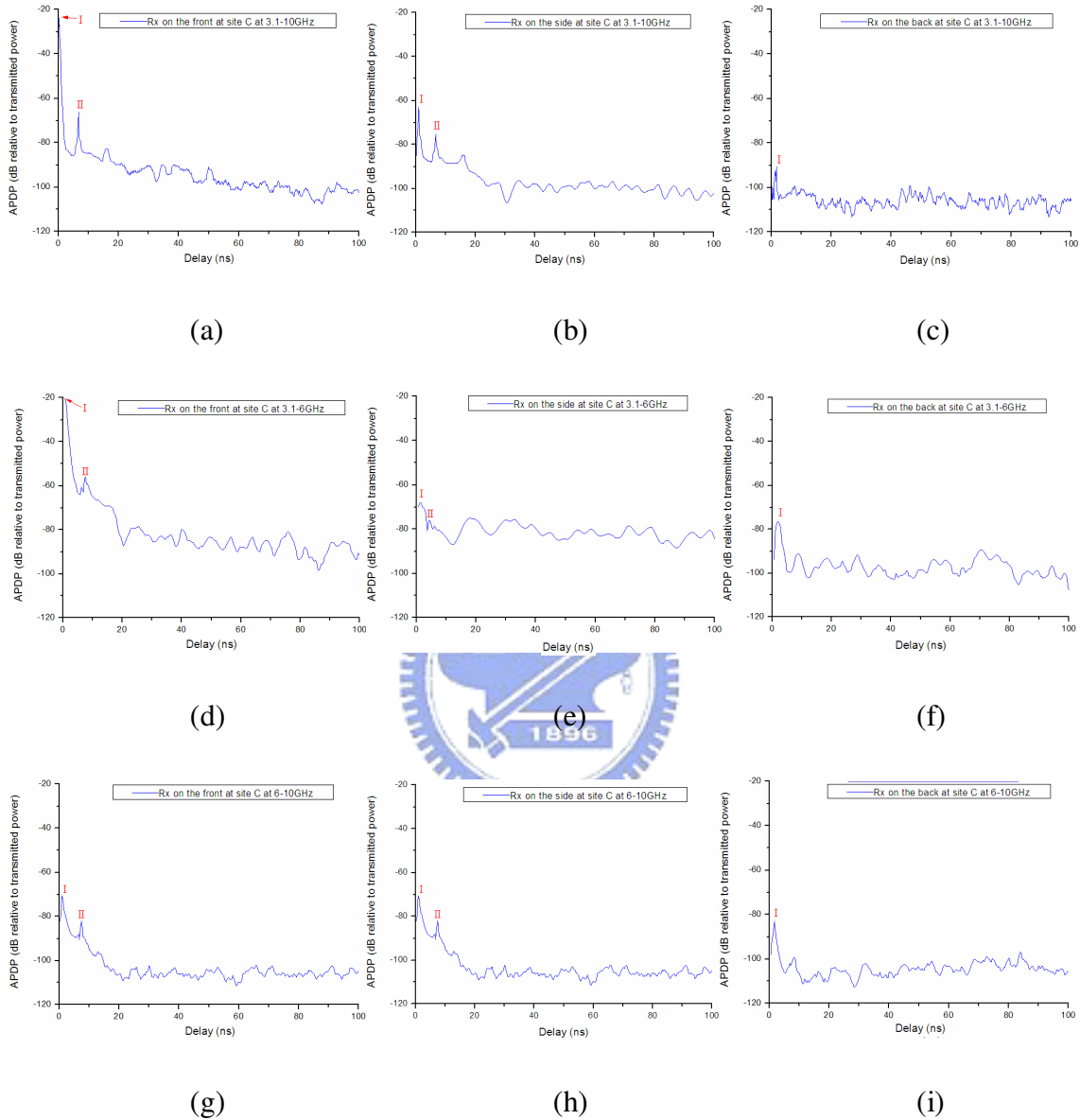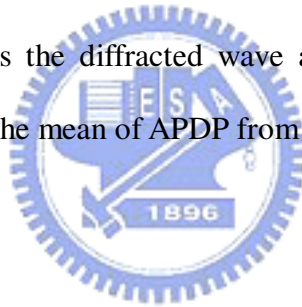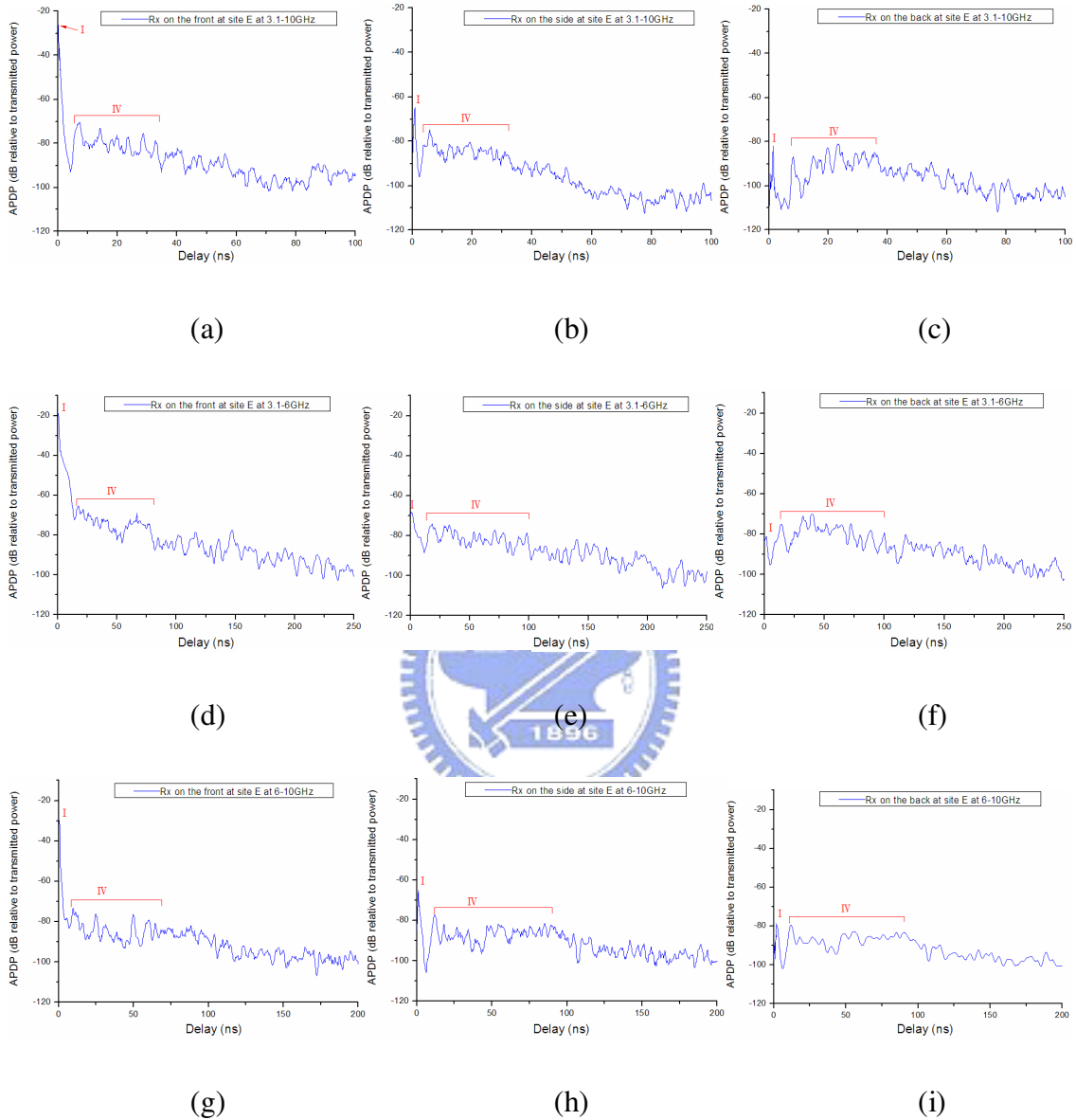
Figure 4.7 APDP versus delay at site E. The receiver placed on the

front of the body at (a)3.1 – 10 GHz, (b)3.1 – 6 GHz, (c)6 – 10 GHz.

side of the body at (d)3.1 – 10 GHz, (e)3.1 – 6 GHz, (f)6 – 10 GHz.

back of the body at (g)3.1 – 10 GHz, (h)3.1 – 6 GHz, (i)6 – 10 GHz

Table 4.4 Mean of APDP from site E

μ_{dB} Receiver Position	3.1-10GHz	3.1-6 GHz	6-10 GHz
front	-26.48	-21.78	-30.7
side	-66.12	-61.8	-69. 9
back	-82	-81.3	-82

4.3 Small Scale fading

To characterize the small-scale statistics by fitting the received energies in each time at site E, the Dual Slope Model, Weibull distribution, Lognormal distribution, Nakagami-m distribution and Rayleigh distribution are used. The Akaike Information Criterion indicates (AIC) the trade off between the complexity of a model and how the model fit well compared.

4.3.1 Dual Slope Model

Traditionally, clusters are assumed to decay exponentially with arrival time. However, the second group of clusters decays more rapidly than the first group and there is significant variance around the average trend. Therefore, the following dual slope model is more appropriate:

$$\overline{G_{dB}}(\tau_l) = \begin{cases} \Gamma_1 \tau + G_\sigma n & \tau_l \le \tau_{bp} \\ \Gamma_1 \tau_{bp} + \Gamma_2 (\tau_1 - \tau_{bp}) + G_\sigma n & \tau_l \ge \tau_{bp} \end{cases}$$

$\overline{G_{dB}}(\tau_l)$ represents the magnitude of the cluster arriving at excess delay τ_l expressed in decibels. Γ_1 and Γ_2 are the cluster decay rates of the first and second group while G_σ is the standard deviation around the average trend. *n* is a unit mean. The cluster decay rates and standard deviation of this model in the three frequency band extracted from our measurements are given in Table 4.5. Figure 4.8 shows the clusters extracted from the measurement taken when the receiver is worn on the front, side and back of the body at the three frequency band, while the vertical axis shows the magnitude of the first time in each cluster corresponding to the cluster peak.

(a)

(b)

(c)

(d)

(e)

(f)

(g)

(h)

(i)

Figure 4.8 Dual Slope Model of observed clusters. Receiver placed on the

(a) front, (b) side, and (c) back of the body at 3.1 – 10 GHz.

(d) front, (e) side, and (f) back of the body at 3.1 - 6 GHz.

(g) front, (h) side, and (i) back of the body at 6 – 10 GHz.

Table 4.5 Parameter of Dual Slope Model

		Front	Side	Back
3.1 – 10 GHz	Γ_1 (dB/ns)	0.148	0.29	0.23
	t_{bp} (ns)	30	30	-
	Γ_2 (dB/ns)	0.51	0.48	-
	G_σ (dB)	2.99	3.53	2.52
	n	-70.4	-76.4524	-81.36
3.1 - 6 GHz	Γ_1 (dB/ns)	0.13	0.21	0.24
	t_{bp} (ns)	30	30	-
	Γ_2 (dB/ns)	0.57	0.45	-
	G_σ (dB)	3	3.1	2.4
	n	-71.43	-75.51	-80.26
6 – 10 GHz	Γ_1 (dB/ns)	0.14	0.26	0.27
	t_{bp} (ns)	30	30	-
	Γ_2 (dB/ns)	0.55	0.43	-
	G_σ (dB)	2.84	2.99	2.31
	n	-71.43	-75.51	-80.26

4.3.2 Weibull Distribution

The details of weibull distribution describes in chapter 2. Figure 4.9 shows the cumulative density function (CDF) for arrival times of clusters in the first cluster group when the receiver placed on the front, side, and back of the body in the three frequency bandwidth. The exponential distribution is often associated with cluster arrival times but it is clear from the dashed line in Figure 4.9 that it provides a poor fit to our data. The Weibull distribution provides a better fit to the data, the solid line in the Figure 4.9 shows the distribution. The Weibull probability density function can be used to determine the cluster arrival times.

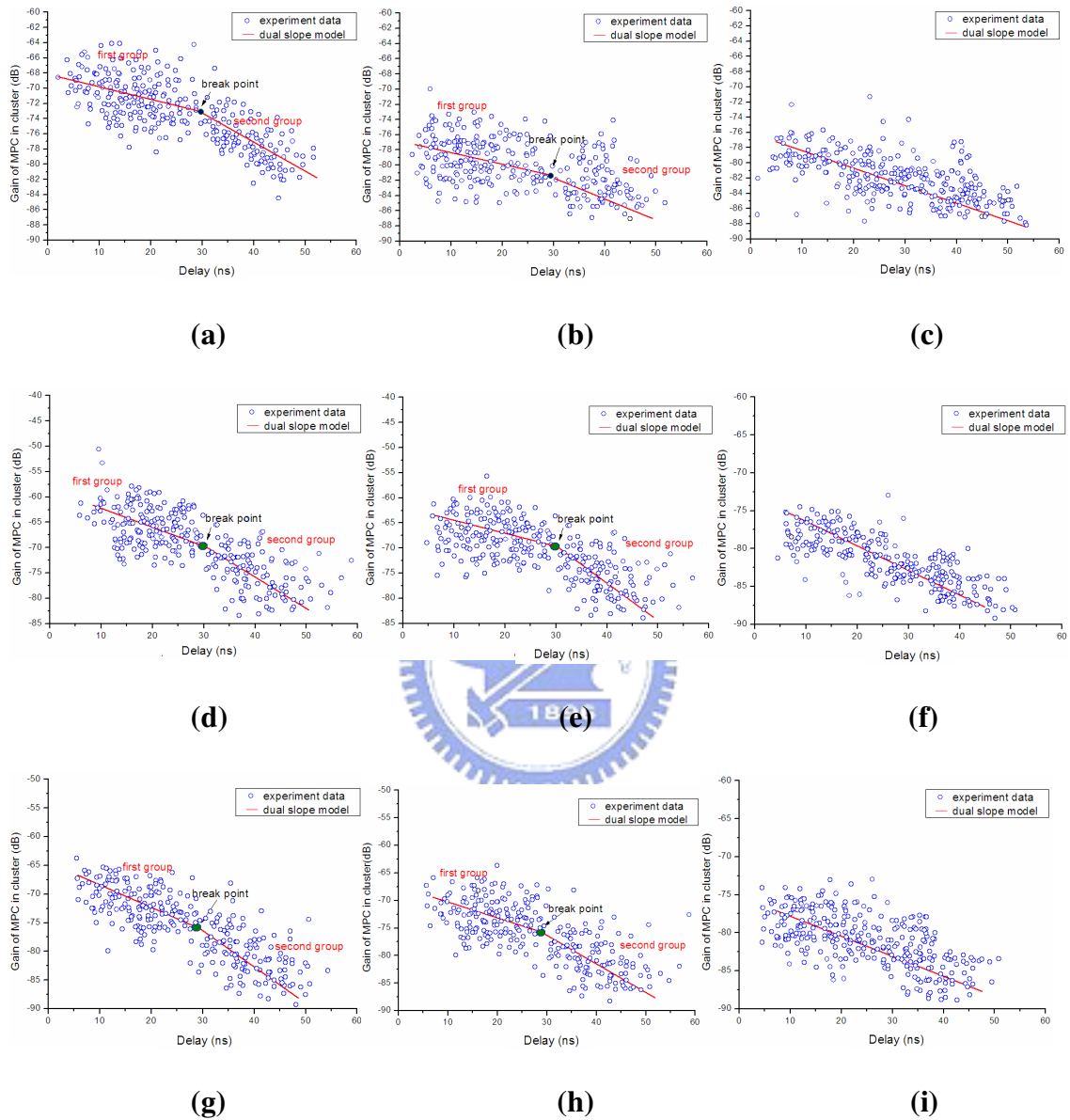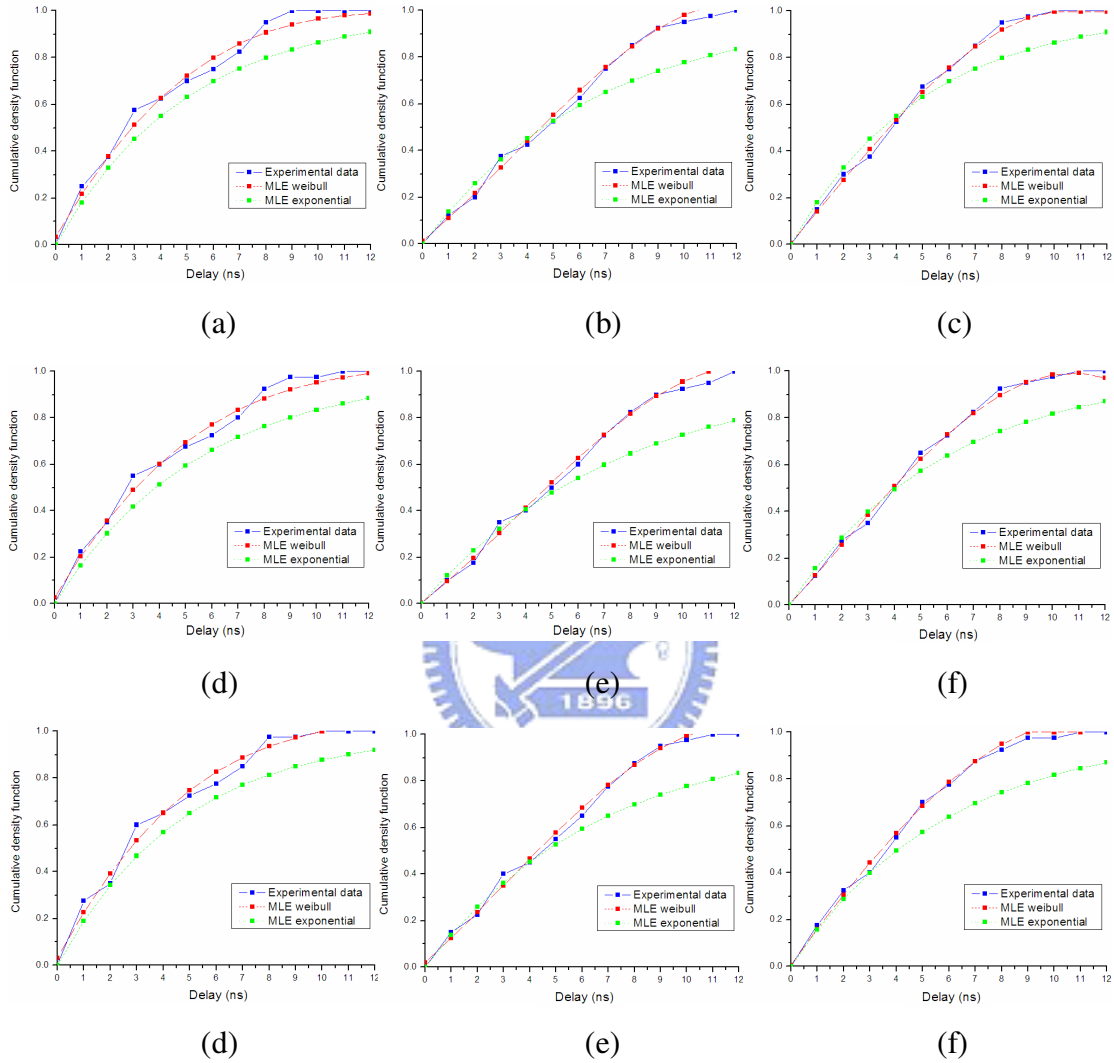**Figure 4.9 CDF versus arrival time of clusters. Receiver placed on the**

(a) front, (b) side, and (c) back of the body at 3.1 – 10 GHz.

(d) front, (e) side, and (f) back of the body at 3.1 - 6 GHz.

(g) front, (h) side, and (i) back of the body at 6 – 10 GHz.

4.3.3 Lognormal, Rayleigh, Nakagami-m Distributions

The details of the three distributions describes in the chapter 2. To observed the three distributions in the Figure 4.10, the Lognormal distribution provides a good fit to the measurement data than others. The average value and standard deviation for the three distributions are given in Table 4.6. While the small scale distribution can be different in each time contributing to the variance, we do not detect significant trends in the parameters for different body positions. The AIC indicates that the Lognormal distribution is the best model in 52.3%, while the Nakagami-m distribution is indicated in 39.9%. In most cases, the Rayleigh distribution has the worst fit to the measured data, and the Lognormal distribution is the best distribution for the small scale around the body. Table 4.7 describes the value of AIC.

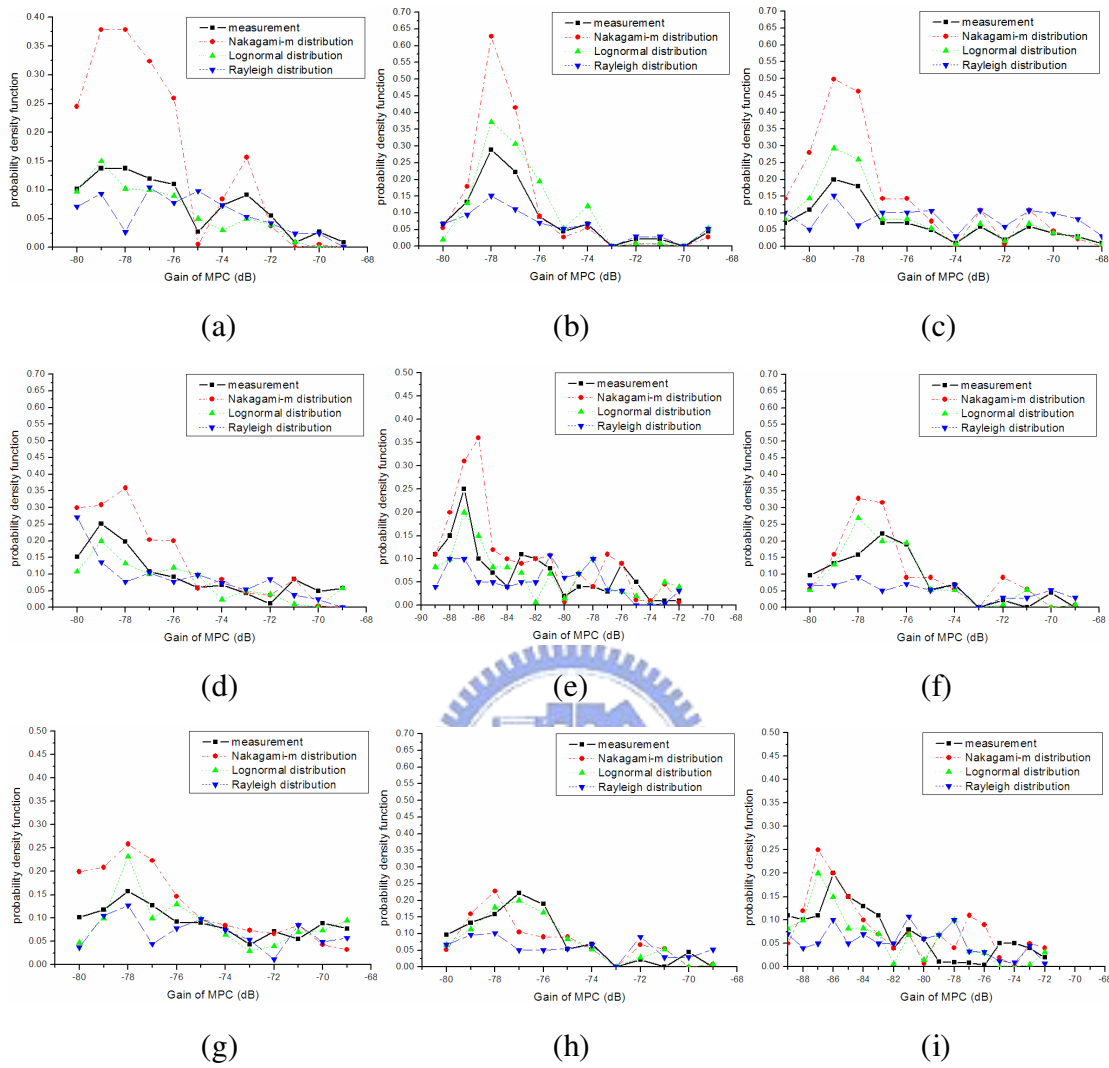**Figure 4.10 Comparison of the measured and modeled PDF. Receiver placed on the**

(a) front, (b) side, and (c) back of the body at 3.1 – 10 GHz.

(d) front, (e) side, and (f) back of the body at 3.1 - 6 GHz.
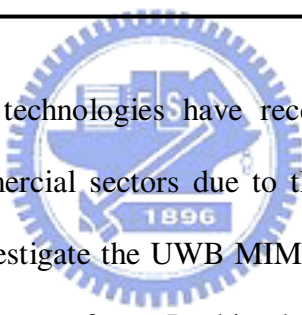
(g) front, (h) side, and (i) back of the body at 6 – 10 GHz.

Table 4.6 the parameters of the measurement data, Lognormal, Nakagami-m, and Rayleigh distribution at three frequency bandwidth.

			Front	Side	Back
3.1 – 10 GHz	measurement	Average Value	0.083	0.083	0.065
	Lognormal	Average Value	0.068	0.106	0.069
		Standard Deviation	0.03	0.05	0.03
	Nakagami-m	Average Value	0.165	0.124	0.11
		Standard Deviation	0.1	0.1	0.075
	Rayleigh	Average Value	0.074	0.036	0.06
		Standard Deviation	0.11	0.1	0.097
3.1 – 6 GHz	measurement	AverageValue	0.08	0.081	0.062
	Lognormal	Average Value	0.061	0.11	0.15
		Standard Deviation	0.02	0.04	0.02
	Nakagami-m	Average Value	0.17	0.15	0.13
		Standard Deviation	0.1	0.2	0.069
	Rayleigh	Average Value	0.06	0.04	0.06
		Standard Deviation	0.12	0.1	0.1
6 – 10 GHz	measurement	Average	0.079	0.08	0.068
	Lognormal	Average Value	0.07	0.12	0.1
		Standard Deviation	0.03	0.05	0.03
	Nakagami-m	Average Value	0.19	0.17	0.14
		Standard Deviation	0.1	0.1	0.075
	Rayleigh	Average Value	0.08	0.05	0.04
		Standard Deviation	0.11	0.1	0.097

Table 4.7 AIC of lognormal, Nakagami-m and Raleigh models

Receiver position	Lognormal	Nakagami-m	Rayleigh
Front	55.03%	45.45%	28.61%
Back	52.6%	34.8%	38.26%
Side	50.69%	40.77%	29.52%

Chapter 5   *Analysis of UWB MIMO BANs' Channel Capacity*

UWB and MIMO radio technologies have recently attracted great interest in scientific, industrial and commercial sectors due to their capabilities to support high data rate transmissions. To investigate the UWB MIMO BANs channel characteristics, an extensive measurements were perform. In this chapter, the effects of propagation condition, antenna spacing and bandwidth on the UWB MIMO channel capacity are analyzed based on the measurement results. It is noted that, the MIMO channel capacity is calculated under 20 dB signal to noise ratio in this paper.

5.1 Propagation Condition Effect

5.1.1 LOS/NLOS Between Transmitting and Receiving Antenna Array

Figures 5.1, 5.2 and 5.3 show the MIMO channel capacities versus number of array elements at Site C, Site D and Site E, respectively. Here, the measured bandwidth is in the range of 3 to 10 GHz, and both the array element spacing at transmitting and

receiving sides are equal to 3 cm.

From these figures, it is found that the channel capacity of MIMO_2 and MIMO_3 scenarios are greater than MIMO_1 and MIMO_4 scenarios. It is because that the transmitting and receiving antenna arrays of MIMO_2 and MIMO_3 scenarios. are in NLOS propagation condition, rich multipath lead to lower correlation between sub-channels and higher capacity than those of MIMO_1 and MIMO_4 scenarios. The average correlation coefficient for 3-cm antenna spacing is equal to 0.6129, 0.3859, 0.1883 and 0.6216 for MIIMO_1, MIMO_2, MIMO_3 and MIMO_4 scenarios, respectively.
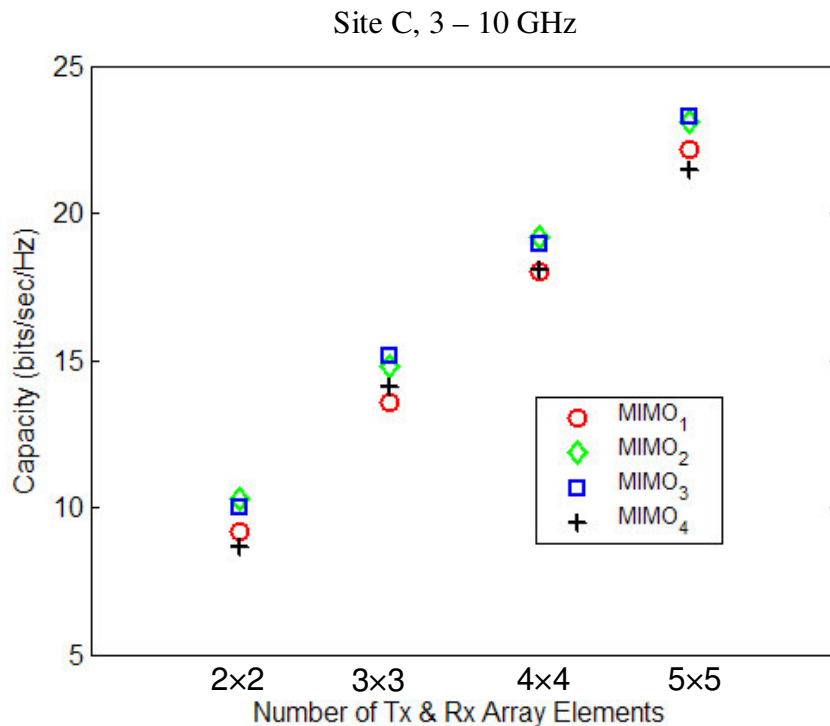
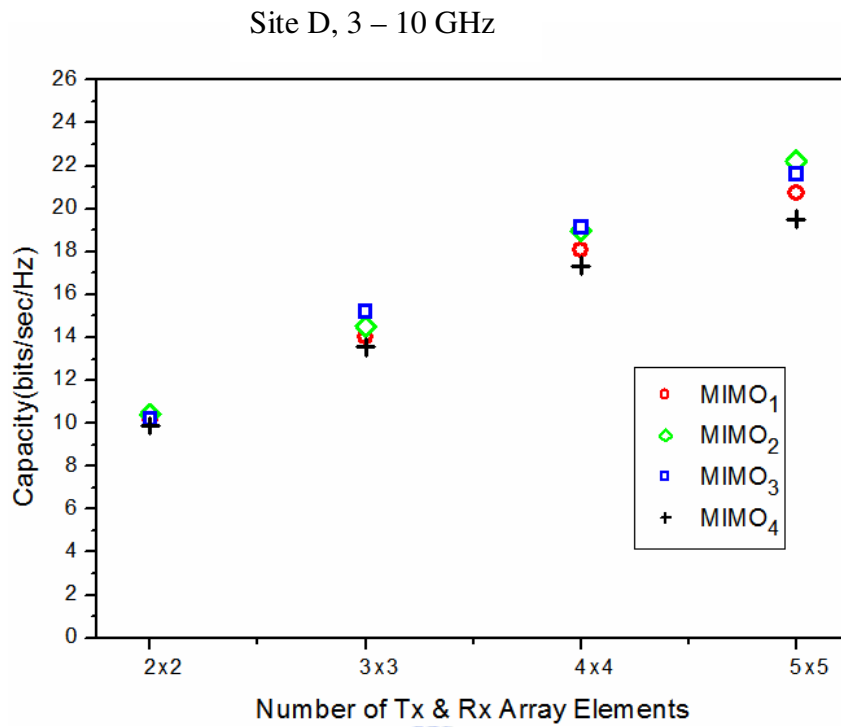**Figure 5.1 MIMO channel capacity versus number of array elements at Site C.**

Site D, 3 – 10 GHz

Figure 5.2 MIMO channel capacity versus number of array elements at Site D.
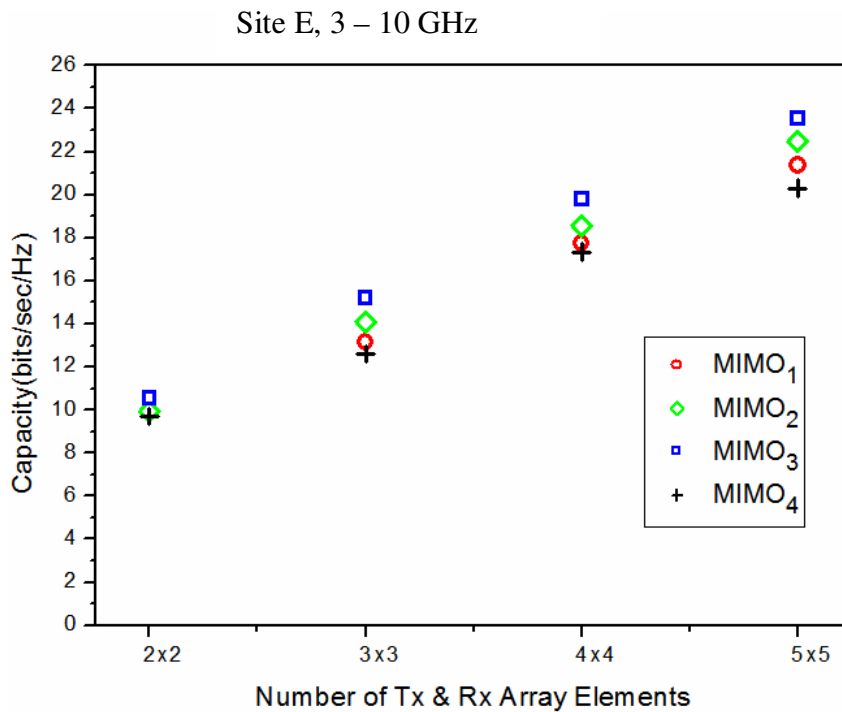
Site E, 3 – 10 GHz

Figure 5.3 MIMO channel capacity versus number of array elements at Site E.

5.1.2 Propagation Environments

Figures 5.4 and 5.5 show the MIMO channel capacities versus number of array elements for MIMO_1 and MIMO_2 scenarios, respectively. Here, the measured bandwidth is in the range of 3 to 10 GHz, and both the array element spacing at transmitting and receiving sides are equal to 3 cm.

From these two figures, it is found that the channel capacity is independent of the propagation environments. For MIMO_1 scenario, it is because that the directed path is much strong compared to the multipath caused by the scatterers inside the building. It means that the MIMO channel capacity is mainly contributed from the directed path between the transmitting and receiving antenna arrays. Therefore, the MIMO channel capacity is independent of propagation environment for MIMO_1 scenario. Same result is also found for MIMO_4 scenario.

For MIMO_2 scenario, since the transmitting and receiving antenna arrays is under NLOS condition, the correlation between sub-channels is low even in Site C, the open space environment. Therefore, the large number of multipath components of Site D and Site E does not give significant contribution on MIMO channel capacity for MIMO_2 scenario. Same result is also found for MIMO_3 scenario.
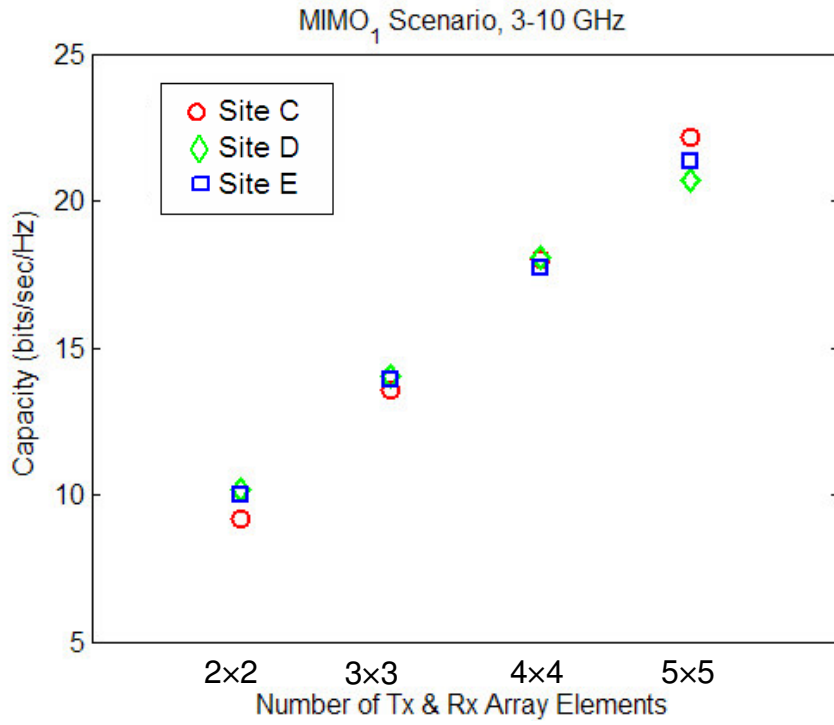
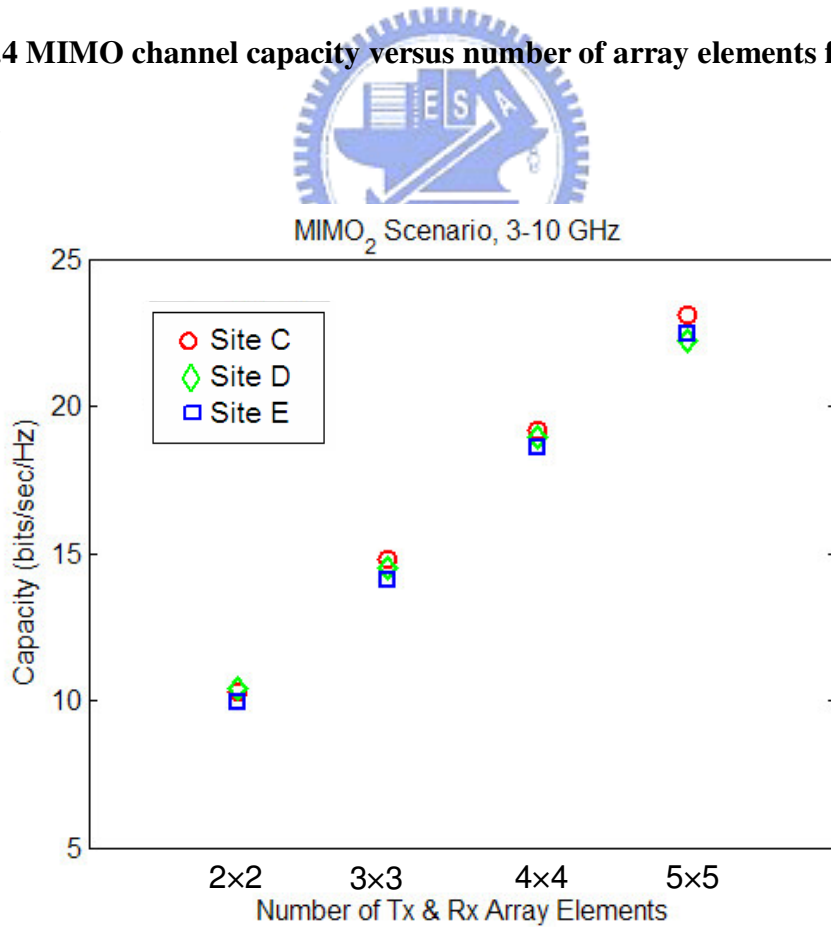**Figure 5.4 MIMO channel capacity versus number of array elements for MIMO_1 scenario.**

Figure 5.5 MIMO channel capacity versus number of array elements for MIMO_2 scenario.

5.2 Antenna Spacing Effect

Figure 5.6 show the 2×2 MIMO channel capacity versus receiving antenna spacing at Site C. Here, the measured bandwidth is in the range of 3 to 6 GHz. From this figure, it is found that the MIMO channel capacity is decreased when the receiving antenna spacing is increased for most of the MIMO propagation scenarios. This phenomenon is not consistent with the results which have been found in local area network (LAN) and wide area network (WAN) environments for MIMO channels.

Figure 5.7 show the spatial correlation coefficient at receiving side versus receiving antenna spacing at Site C. From this Figure, it is found that the spatial correlation coefficient at receiving side is decreased when the receiving antenna spacing is increased. It is consistent with the results which have been found in LAN and WAN environments. However, it is not reasonable to explain why the MIMO channel capacity is decreased when the receiving antenna spacing is increased.

The result shown in Figure 5.8 may give an reasonable answer to explain this phenomenon. Figure 5.8 show the maximum power difference among the sub-channels versus the antenna spacing at receiving and transmitting sides. It is found that the maximum power difference among the sub-channels is increased when the antenna spacing is increased. For MIMO technologies, maximum channel capacity is achieved when the sub-channels are uncorrelated and with equal mean power. When some sub-channels' power are very low compared to others', these low power sub-channels does not contribute to the MIMO channel capacity even they are uncorrelated to others. For BAN, the distance between transmitting and receiving antennas is small. Therefore, when the antenna spacing is increased, the differences of propagation distance between sub-channels is increased, which leads to the decreased MIMO channel capacity.

Same results can be found in Site D and Site E. Figures 6.9, 6.10 and 6.11 show the channel capacity, the spatial correlation coefficient and the maximum power difference versus antenna spacing, respectively, at Site D.

Figures 5.12, 5.13 and 5.14 show the channel capacity, the spatial correlation coefficient and the maximum power difference versus antenna spacing, respectively, at Site E.
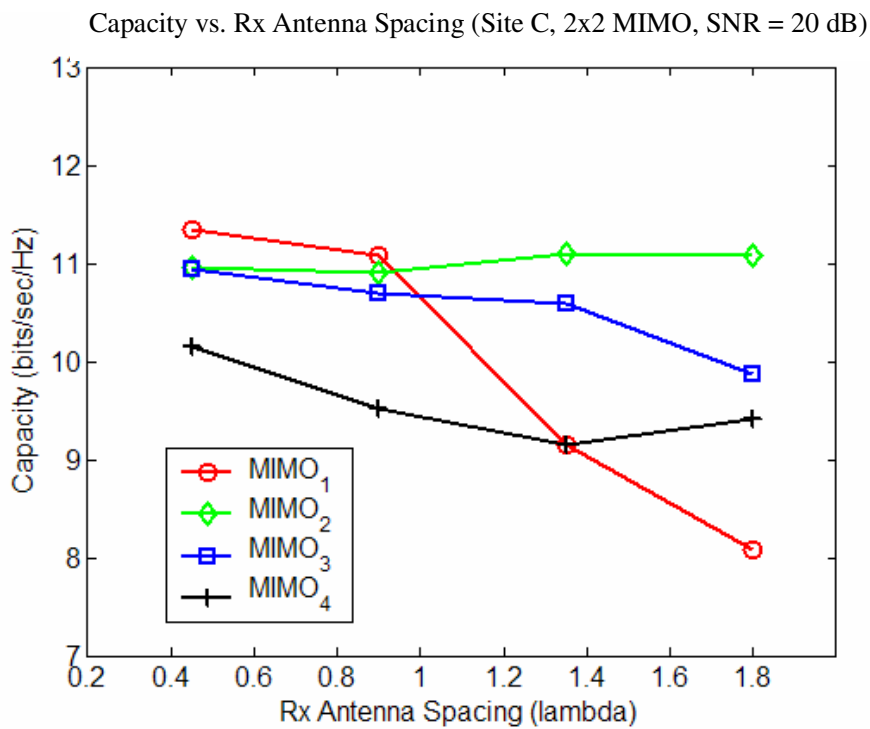

Figure 5.6 MIMO channel capacity versus receiving antenna spacing at Site C.
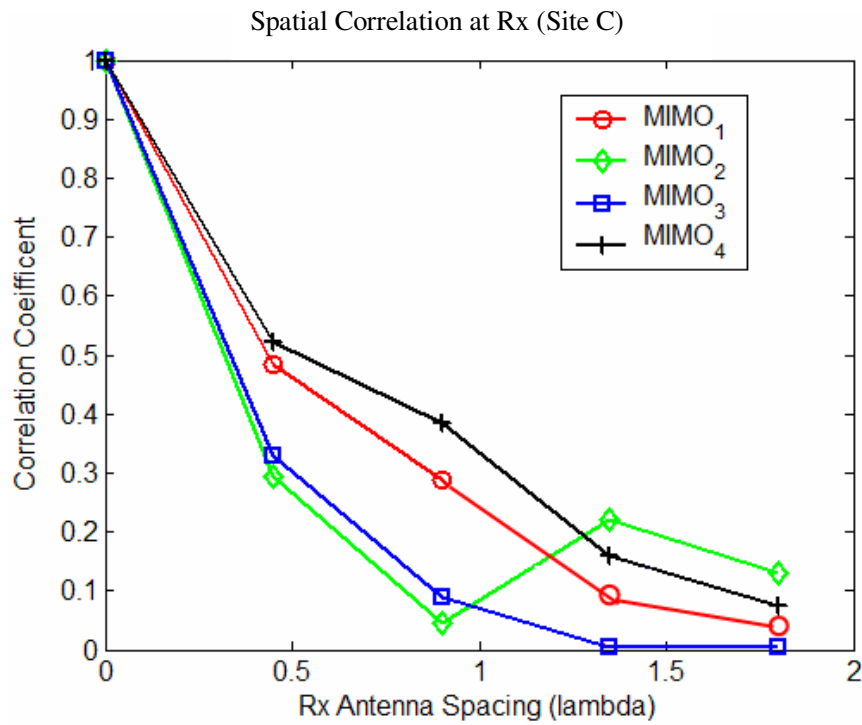
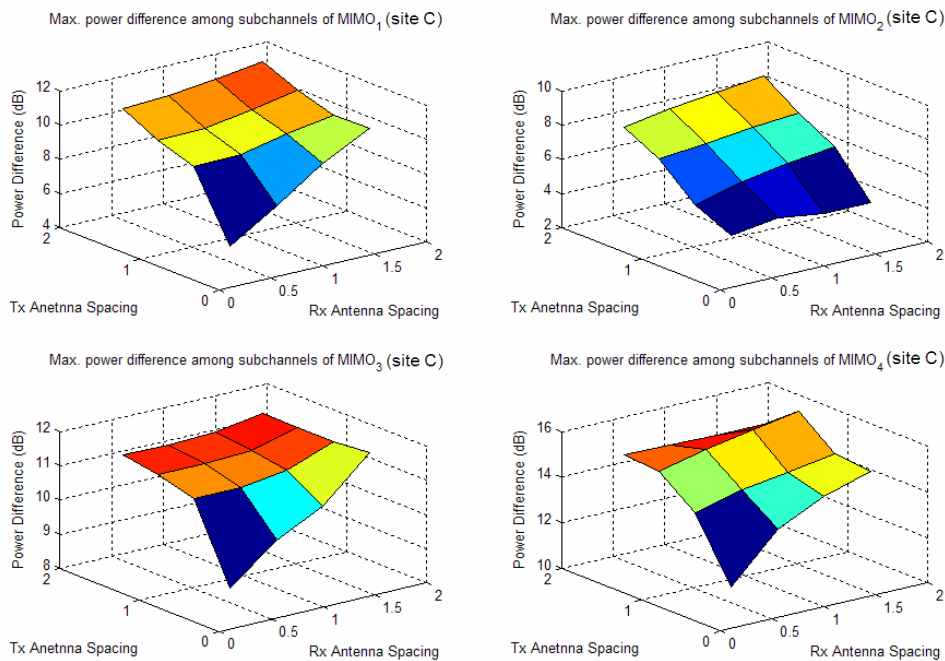**Figure 5.7 Spatial correlation coefficient versus receiving antenna spacing at Site C.**

Figure 5.8 Maximum power difference among sub-channels versus receiving and transmitting antenna spacing at Site C.

Capacity vs. Rx Antenna Spacing (Site D, 2x2 MIMO, SNR = 20 dB)

Figure 5.9 MIMO channel capacity versus receiving antenna spacing at Site D.

Spatial Correlation at Rx (Site D)

Figure 5.10 Spatial correlation coefficient versus receiving antenna spacing at Site D.

Figure 5.11 Maximum power difference among sub-channels versus receiving and transmitting antenna spacing at Site D.

Figure 5.12 MIMO channel capacity versus receiving antenna spacing at Site E.

Spatial Correlation at Rx (Site E)

Figure 5.13 Spatial correlation coefficient versus receiving antenna spacing at Site E.

Figure 5.14 Maximum power difference among sub-channels versus receiving and transmitting antenna spacing at Site E.
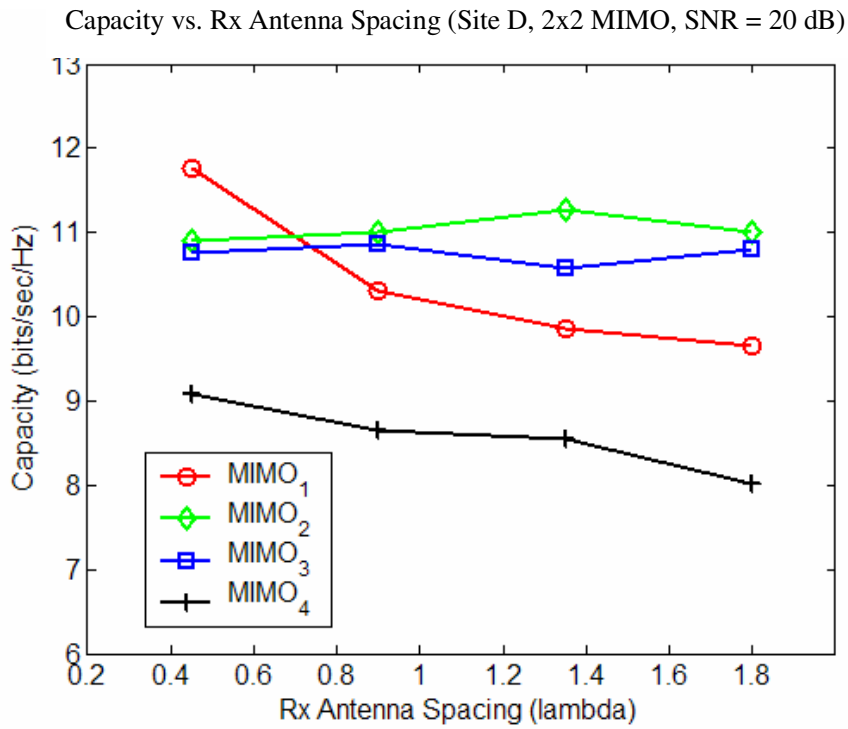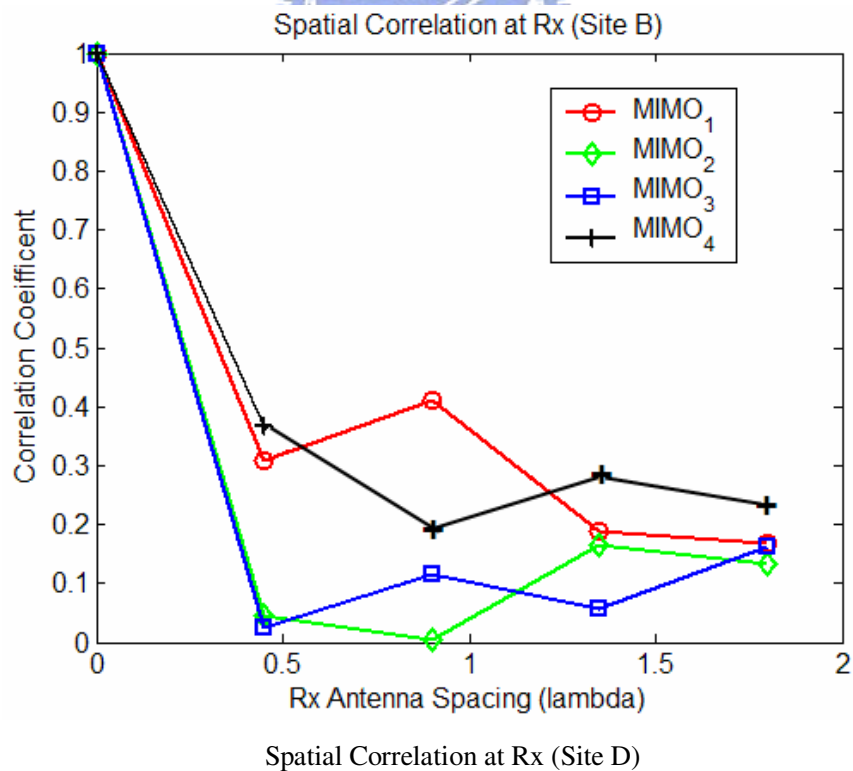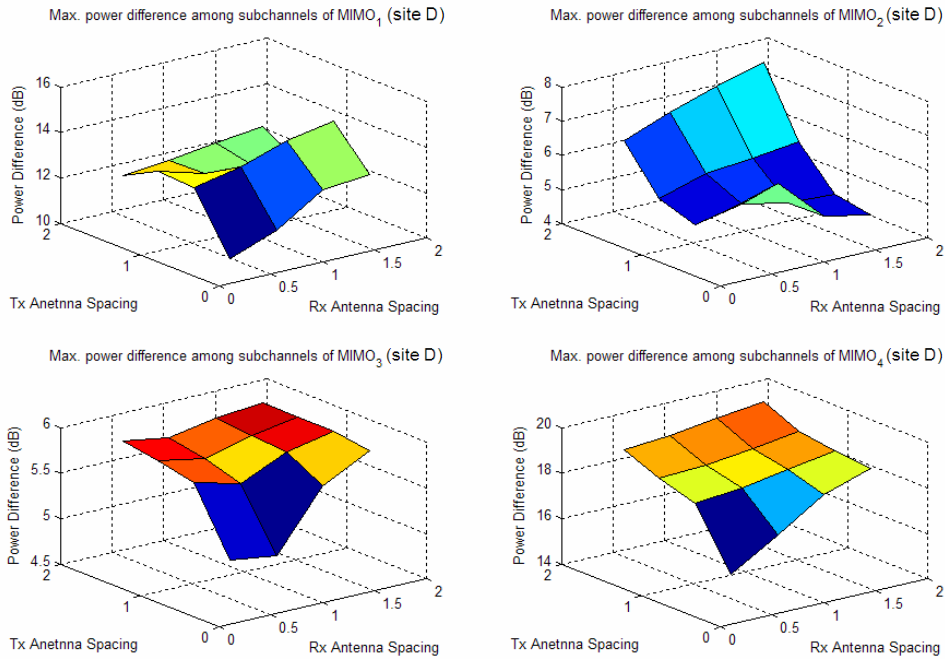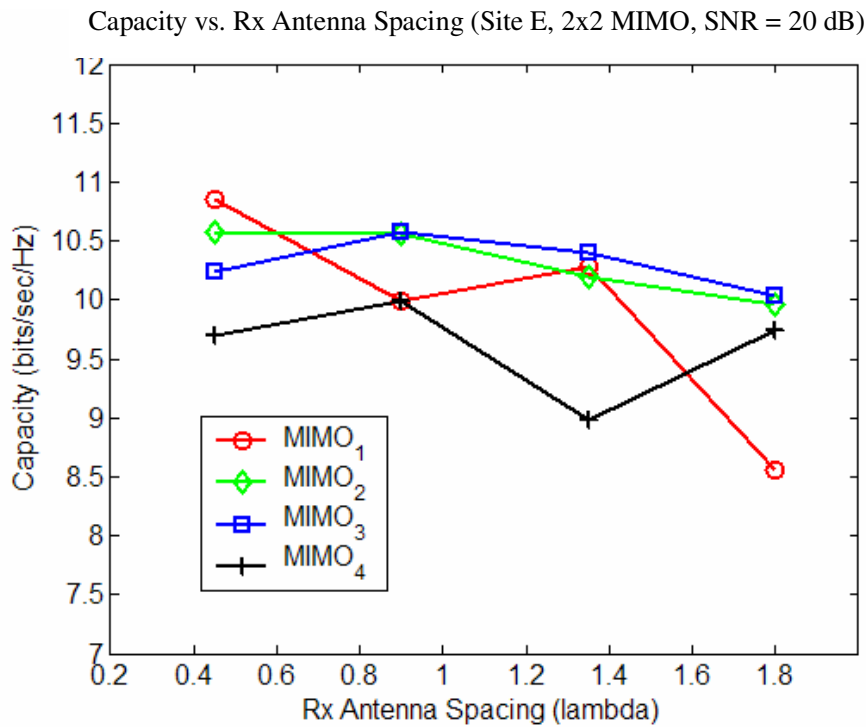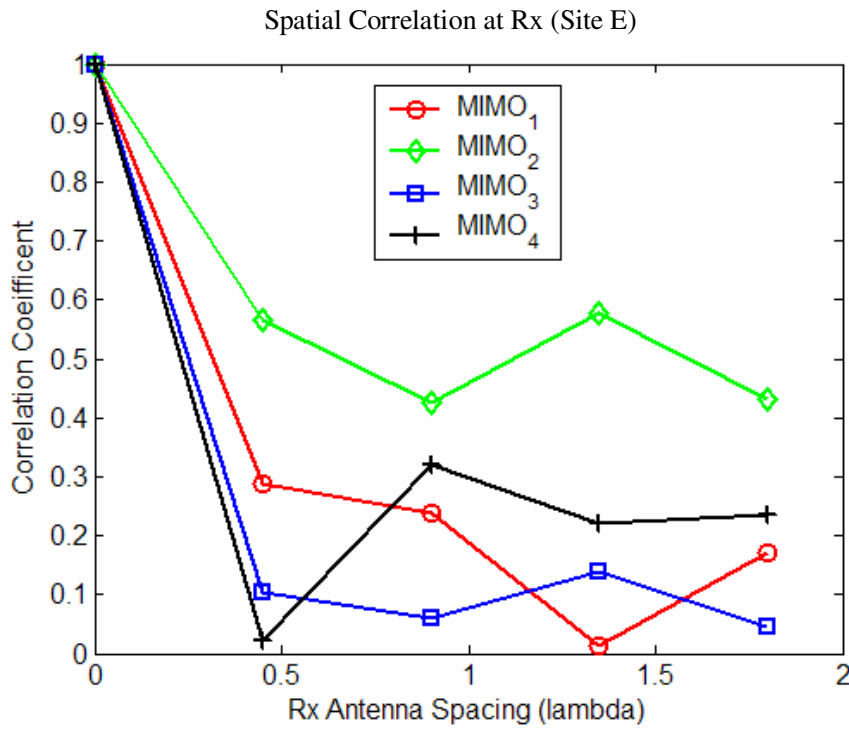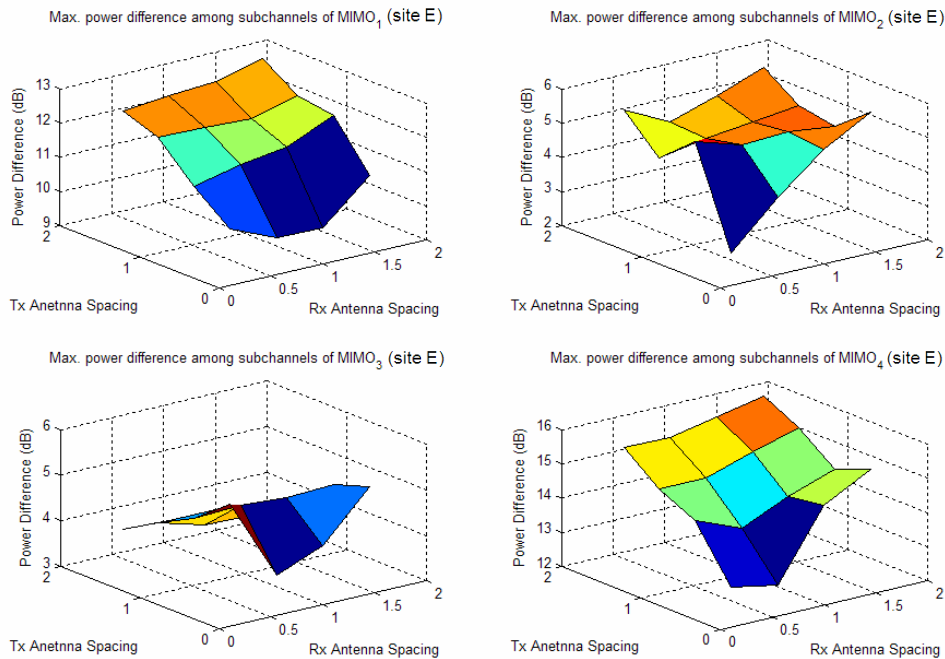
5.3 Bandwidth Effect

Figures 5.15 and 5.16 show the MIMO channel capacity versus frequency band for MIMO_1 and MIMO_2 scenario, respectively. Here, the number of antenna array elements is 2×2, and the antenna spacing is 3 cm.

From these figures, it is found that the MIMO channel capacity decreased with frequency and bandwidth. It is because that the frequency response power is decreased when the frequency band increased, which can be found in Figures 5.17, 5.18 and 5.19. For UWB MIMO, the channel capacity is equal to the average of the multiple narrowband channel capacity. Therefore, high frequency components do not contribute to the channel capacity due to its low power compared to the low frequency components.

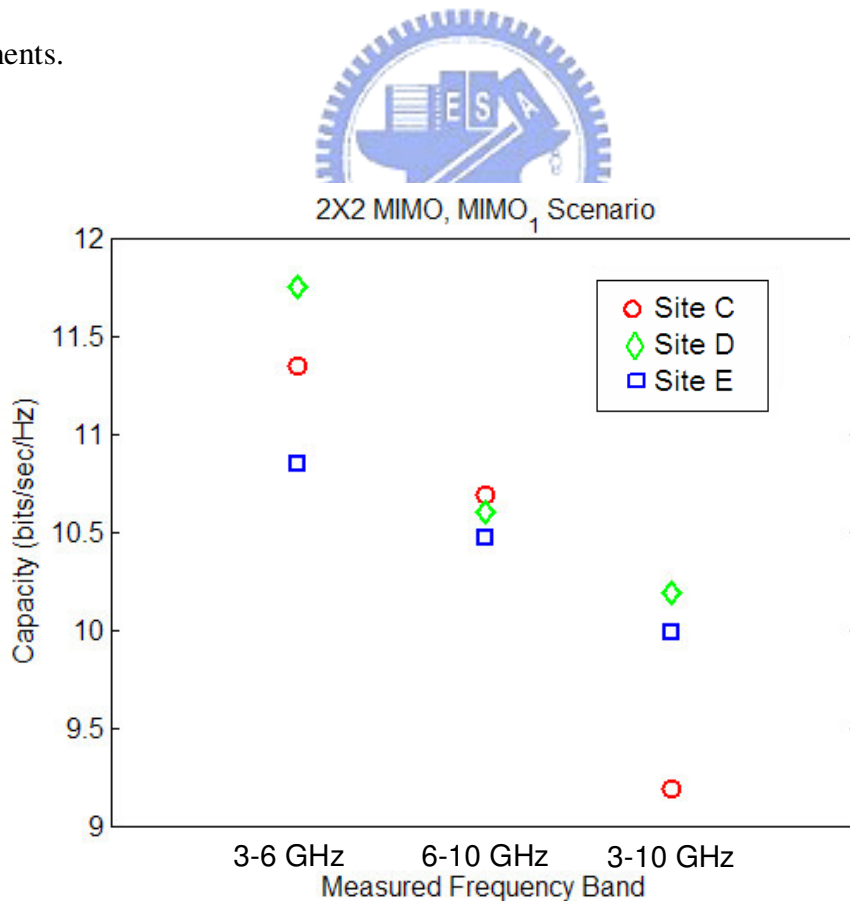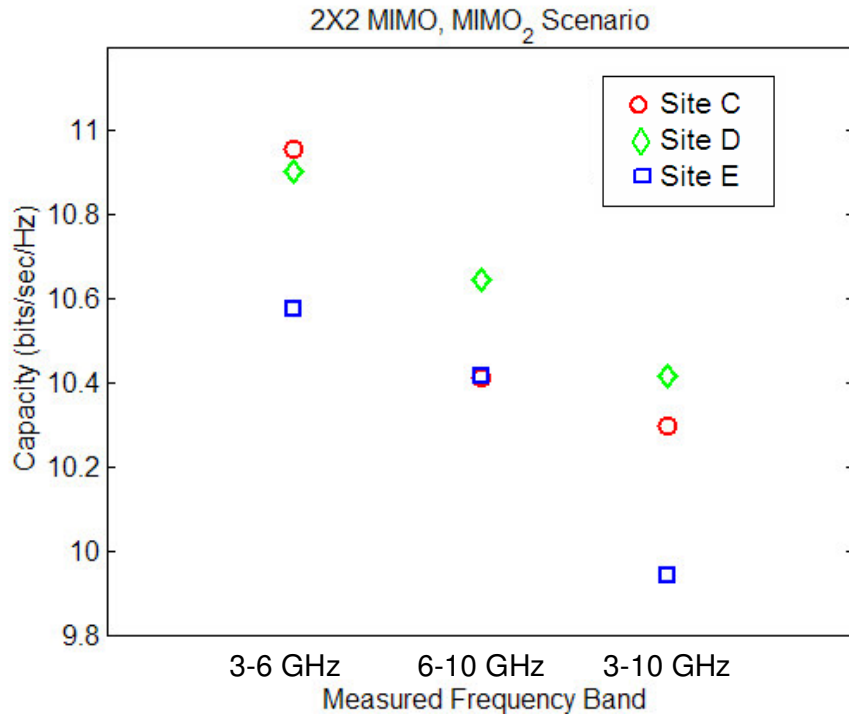**Figure 5.15 MIMO channel capacity versus frequency band for MIMO_1 scenario.**

Figure 5.16 MIMO channel capacity versus frequency band for MIMO_2 scenario.

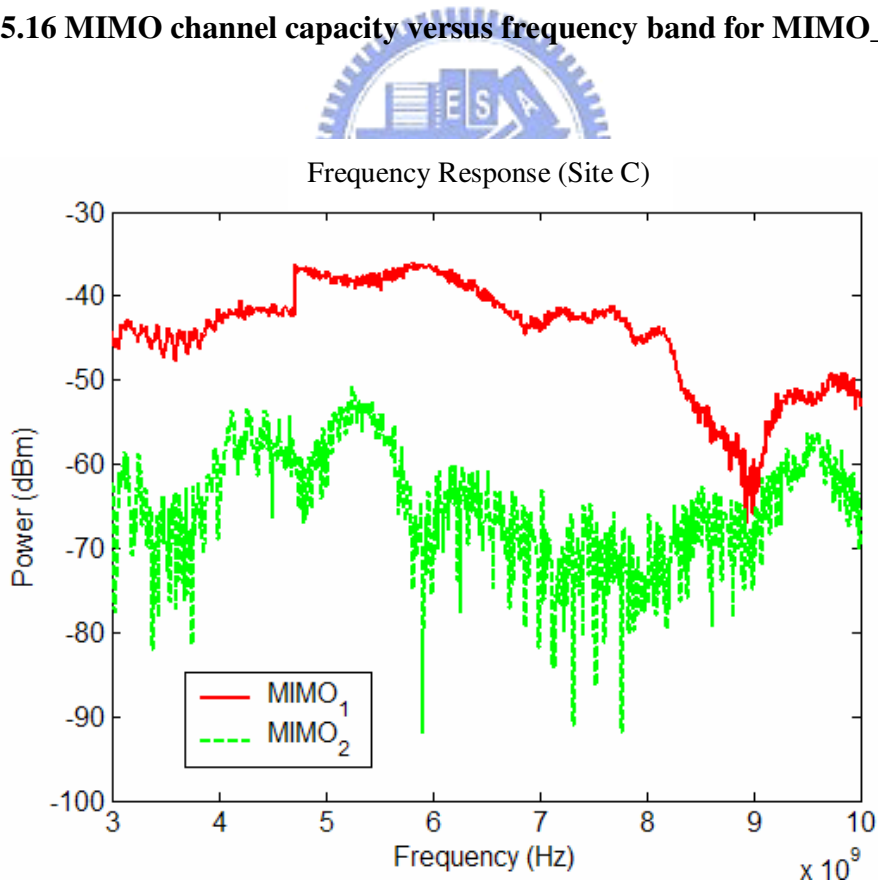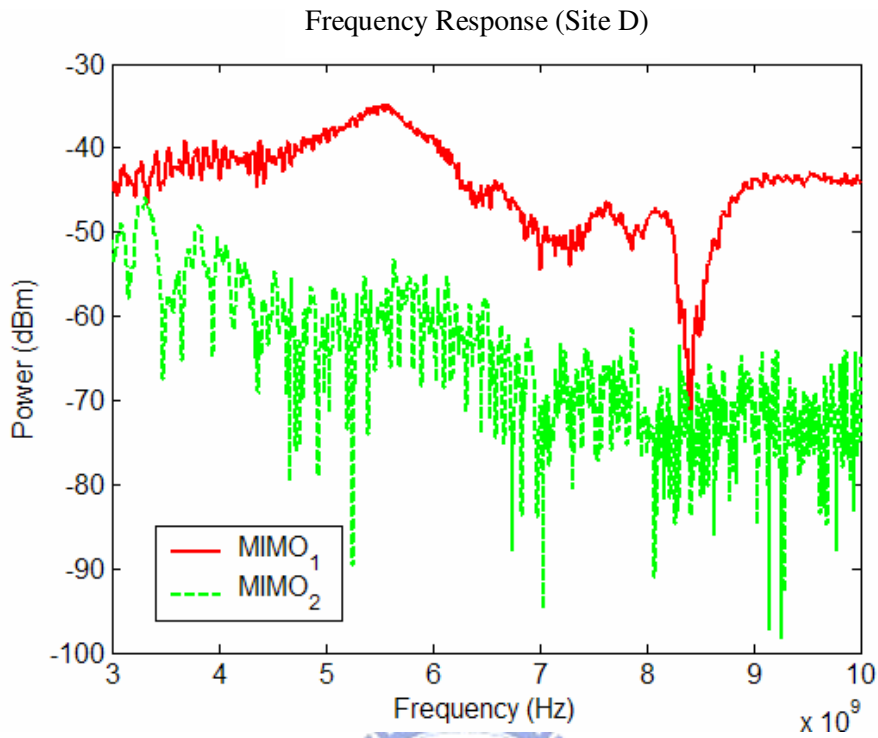**Figure 5.17 One sub-channel frequency response at Site C.**

Frequency Response (Site D)

Figure 5.18 One sub-channel frequency response at Site D.
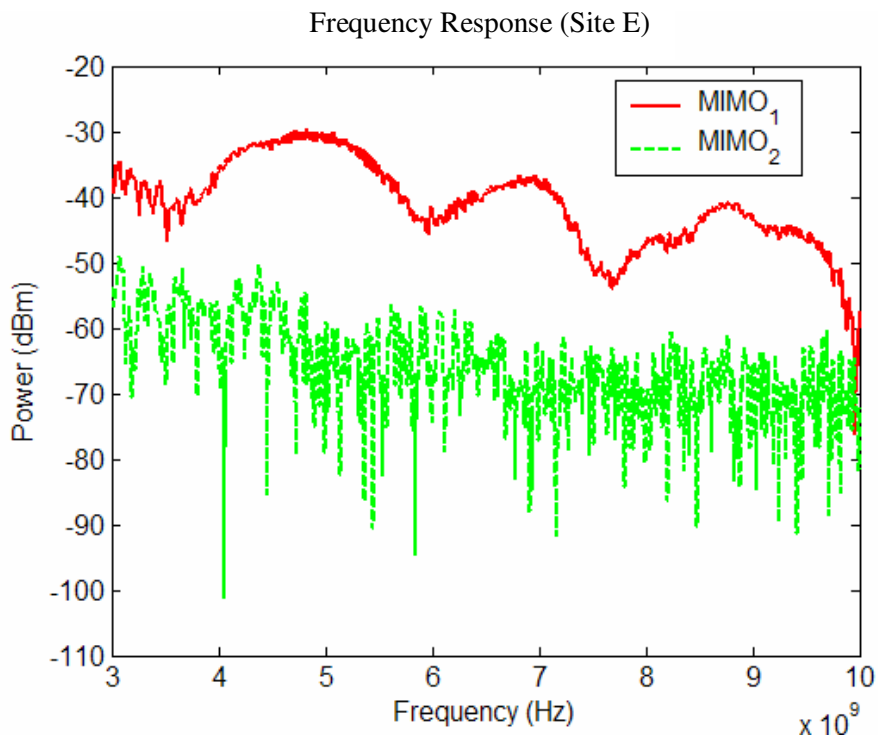
Frequency Response (Site E)
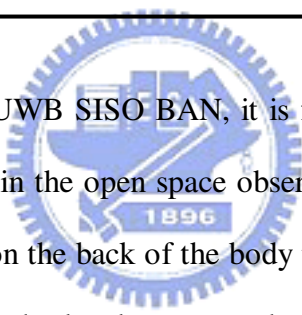
Figure 5.19 One sub-channel frequency response at Site E.

Chapter 6   Conclusion

For channel modeling of UWB SISO BAN, it is found that the diffracted wave is the dominant propagation path in the open space observed from the temporal response. However, when the Rx places on the back of the body that is surrounded by dense local scatterers, the scattering due to the local scatterers becomes the dominant propagation mechanism and the received signal strength is much larger than that of without local scatterers. Therefore, the path loss exponent in the room with dense local scatterers is smaller than that in open space. The AIC indicates that the Lognormal distribution is the best one in modeling the small scale fading distribution to compare with the Dual Slope Model, Nakagami-m, Rayleigh and Weibull distributions. It is noted that the Rayleigh distribution is acceptable, which is different from [3].

For MIMO BAN measurement, the capacity of Rx antenna array elements placed on the back of the body is higher than that placed on the front of the body. This is due to the received signal obstructed by the body, which yields reduction of the spatial channel

correlation at the Rx antenna. The influence of environment on the capacity of BAN MIMO system is not significant. However, the capacity of Rx placed on the front of the body is more easy affected by the local environment than that placed on the back of the body. It is found that the capacity of the MIMO BAN decreases as the element spacing increases. It is because that although the increasing element spacing may reduce the correlation of Rx or Tx and leads capacity increase, the signal strength of the subchannel decreases a lot due to large diffraction loss and yields little contribution of the subchannel. Therefore, element spacing increases may not contribute to the MIMO channel capacity.

REFERENCES

[1] http://standards.ieee.org/board/nes/projects/802-15-4a.pdf

[2] J. Ryckaert, P. De Doncker, R. Meys, A. de Le Hoye, S. Donnay, "Channel model for wireless communication around human body", ELECTORONICS LETTERS 29th, vol. 40, No. 9, April 2004

[3] A. Fort, J. Ryckaert, C. Desset, P. DeDoncker, P. Wambacq, L. Van Biesen, " Ultra Wide-band Channel Model for Communication Around the Human Body", IEEE Journal on Selected Areas in Communications, vol. 24, no. 4, April 2006

[4] T. Zasowski, G. Meyer, F. Althaus, A. Wittneben, "Propagation Effects in UWB Body Area Networks", Ultra-Wideband, IEEE International Conference, 2005

[5] A. Fort, C. Desset, P. DeDoncker, P. Wambacq, L. Van Biesen, "An Ultra-Wideband Body Area Propagation Channel Model—Form Statistics to Implementation", IEEE Transactions on Microwave Theory and Techniques", vol. 54, no. 4, April 2006

[6] A. Alomainy, Y. Hao, CG Parini, PS Hall, "UWB on-body radio propagation and system modeling for wireless body-centric networks", IEE Proc.-Commun., vol. 153, no. 1, February 2006

[7] 羅信文,「新型縮小化超寬頻印刷式天線設計」,國立交通大學,碩士學位,2004

[8] 蔡孟勳,「超寬頻多輸入多輸出系統模型之建構與量測」,國立交通大學,碩士學位,2005

[9] A. F. Molisch, et al., "IEEE 802.15.4a channel model - final report", IEEE P802. 15 Working Group for WPANs, 2004

[10] Norman Morrison, <u>Introduction to Fourier analysis /with full-system FFT disk</u>, Wiley, New York, 1994

[11] Alberto Leon-Garcia, <u>Probability and random processes for electrical engineering</u>, Second Edition, Addison-Wesley, 1994

[12] Bhaskar Krishnamachari, <u>Networking Wireless Sensors</u>, Cambridge University Press, January 2006

[13] Theodore S. Rappaport, <u>Wireless Communications: principles and practice</u>, Second Edition, Prentice Hall Communications Engineering and Emerging Technologies Series, 2002

[14] Warren L. Stutzman, Gary A. Thiele, <u>ANTENNA THEORY AND DESIGN</u>, Second Edition, John Wiley & Sons, New York, 1998

[15] Jose A. Gutierrez, Edgar Callaway, Raymond Barrett, <u>Low-Rate Wireless Personal Area Networks: Enabling Wireless Sensors with IEEE 802.15.4™</u>, Standards Information Network IEEE Press, New York, 2004

[16] 許績偉著，<u>解構短距離無線通訊發展現況與未來趨勢/The current status and future development for wireless personal area network</u>，工業技術研究產業經濟與資訊服務中心出版，新竹縣竹東鎮，2003

[17] 鄭錦聰編著，<u>MATLAB程式設計基礎篇</u>，全華科技圖書股份有限公司，2001

[18] 莊鎮嘉,鄭錦聰編著，<u>MATLAB程式設計實務</u>，全華科技圖書股份有限公司，2006

[19] 洪維恩著，<u>Matlab7程式設計</u>，旗標出版股份有限公司，2006

[20] Y. Zhao, Y. Hao, A. Alomainy, C. Parini, "UWB On-Body Radio Channel Modeling Using Ray Theory and Subband FDTD Method", IEEE Transactions on Microwave Theory and Techniques, vol. 54, no. 4, April 2006

[21] Kyritsi, P.; Cox, D.C, "Correlation Properties of MIMO Radio Channels for Indoor Scenarios," Signals, Systems and Computers, 2001 Conference Record of the

[22] P.S. Hall, M. Ricci, T.W. Hee, "CHARACTERIZATION OF ON-BODY

COMMUNICATION CHANNELS", 3rd International Conference on Microwave and Millimeter Wave Technology Proceedings, 2002

[23] D. Neirynck, C. Williams, A.R. Nix, M.A. Beach, "Personal Area Networks with Line-of-Sight MIMO Operation", IEEE 63rd Vehicular Technology Conference, 2006

[24] J.A. Ruiz, S. Shimamoto, "Experimental Evaluation of Body Channel Response and Digital Modulation Schemes for Intra-body Communications", IEEE International Conference, 2006

[25] J. Wang, D. Su, "Design of an Ultra Wideband System for In-Body Wireless Communications", 4th Asia-Pacific Conference, 2006

[26] A.F. Molisch, K. Balakrishnam, D. Cassioli, C.C. Chong, S. Emami, A. Fort, J. Karedal, J. Kunisch, H. Schantz, K.Siwiak, "A Comprehensive Model for Ultrawideband Propagation Channels", 4th Asia-Pacific Conference, 2006

[27] S.Y. Suh, W.L. Stutzman, W.A. Davis " A New Ultrawideband Printed Monopole Antenna: The Planar Inverted Cone Antenna", 2004 IEEE

[28] Alan V. Oppenheim, Ronald W., Wchafer, Discrete-Time Signal Processing, Prentice hall, 1999

[29] Haykin, "Communication System"Wiley,2001